CLIMATOLOGY

Australia's Tinderbox Drought: An extreme natural event likely worsened by human-caused climate change

Anjana Devanand[1,2]*†, Georgina M. Falster[3,4], Zoe E. Gillett[1,2], Sanaa Hobeichi[1,2], Chiara M. Holgate[3,4], Chenhui Jin[5,6], Mengyuan Mu[1,2], Tess Parker[5,6]‡, Sami W. Rifai[1,2,7], Kathleen S. Rome[1,2], Milica Stojanovic[8], Elisabeth Vogel[1,9,10], Nerilie J. Abram[3,4], Gab Abramowitz[1,2], Sloan Coats[11], Jason P. Evans[1,2], Ailie J. E. Gallant[5,6], Andy J. Pitman[1,2], Scott B. Power[5,6,12,13], Surendra P. Rauniyar[14], Andréa S. Taschetto[1,2], Anna M. Ukkola[1,2]

We examine the characteristics and causes of southeast Australia's Tinderbox Drought (2017 to 2019) that preceded the Black Summer fire disaster. The Tinderbox Drought was characterized by cool season rainfall deficits of around −50% in three consecutive years, which was exceptionally unlikely in the context of natural variability alone. The precipitation deficits were initiated and sustained by an anomalous atmospheric circulation that diverted oceanic moisture away from the region, despite traditional indicators of drought risk in southeast Australia generally being in neutral states. Moisture deficits were intensified by unusually high temperatures, high vapor pressure deficits, and sustained reductions in terrestrial water availability. Anthropogenic forcing intensified the rainfall deficits of the Tinderbox Drought by around 18% with an interquartile range of 34.9 to −13.3% highlighting the considerable uncertainty in attributing droughts of this kind to human activity. Skillful predictability of this drought was possible by incorporating multiple remote and local predictors through machine learning, providing prospects for improving forecasting of droughts.

INTRODUCTION

Human-caused climate change results in changes in the distribution of average rainfall across the globe, as well as amplification of the intensity of wet extremes and droughts (*1*, *2*). Warming over land is also driving an increase in atmospheric moisture demand that has the potential to further increase the likelihood and severity of droughts (*1*). Many regions have experienced an increase in observed drought intensity and frequency over the last few decades, particularly in mid-latitude regions of the northern and southern hemispheres, which support large proportions of the world's population and agricultural food security (*2*). There has also been an observed increase in compound events involving concurrent heatwaves with droughts (*1*). It is possible that drought characteristics are also changing, for example, through the recently identified phenomenon of "flash droughts" that have rapid onset and intensification (*3*). At the same time, paleo records identify multi-year to decadal "megadroughts" that were more intense and longer than any drought experienced during the instrumental period, indicating that far worse droughts are possible even without human-caused drought intensification. Future climate change simulations indicate that droughts will intensify in many regions with global warming, and that every fraction of a degree of additional climate warming can worsen the severity and frequency of droughts in already drought-prone regions (*1*).

Despite the potentially devastating impact of droughts (*4*, *5*), the causes and predictability of individual drought events are usually poorly understood (*6*, *7*). This is partly because each event is unique and involves multiple interacting components of the climate system, and because the observational record provides very few examples of multi-year drought to study. Furthermore, current global climate models have limited skill in replicating multi-year droughts (*8*). Divergence of drought projections across multimodel ensembles also currently limits confidence in projected changes in many regions (*9*, *10*). The multifaceted nature and impacts of droughts means that these climate extremes cannot be adequately understood using single and standardized global metrics applied to observations or climate simulations. Instead, detailed analysis of high-impact case studies provides an alternate approach to advance our understanding of droughts.

Southeast Australia is a naturally drought-prone region and experienced a severe multi-year drought during 2017–2019. It was the driest 3-year period since comprehensive instrumental records began in 1911 (*11*–*13*) and demonstrated the potential for drought events to contribute to cascading and compounding impacts across socio-economic and natural sectors (*14*). The 2017–2019 drought brought rural townships to the brink of running out of water (*15*), caused severe agricultural losses (*16*), and threatened the water supply of Australia's largest city, Sydney (*17*). The drought culminated in catastrophic forest fires in the spring and summer of 2019/2020 that burnt more than 5.8 million hectares of forest (*13*, *18*). The fires were unprecedented in the historical record for their spatial extent, radiative power, and the number of extreme pyroconvective events

---

[1]ARC Centre of Excellence for Climate Extremes, University of New South Wales, Sydney, NSW, Australia. [2]Climate Change Research Centre, University of New South Wales, Sydney, NSW, Australia. [3]ARC Centre of Excellence for Climate Extremes, The Australian National University, Canberra, ACT, Australia. [4]Research School of Earth Sciences, The Australian National University, Canberra, ACT, Australia. [5]ARC Centre of Excellence for Climate Extremes, Monash University, Melbourne, VIC, Australia. [6]School of Earth, Atmosphere and Environment, Monash University, Melbourne, VIC, Australia. [7]School of Biological Sciences, University of Adelaide, Adelaide, SA, Australia. [8]Centro de Investigación Mariña, Universidade de Vigo, Environmental Physics Laboratory (EPhysLab), Campus As Lagoas s/n, Ourense 32004, Spain. [9]Water Research Centre, School of Civil Engineering, University of New South Wales, Sydney, NSW, Australia. [10]Melbourne Climate Futures, The University of Melbourne, Parkville, VIC, Australia. [11]Department of Earth Sciences, University of Hawai'i at Mānoa, Honolulu, HI, USA. [12]Centre for Applied Climate Sciences, University of Southern Queensland, Toowoomba, QLD, Australia. [13]Climate Services International, Oakleigh, Melbourne, VIC, Australia. [14]Australian Bureau of Meteorology, Melbourne, VIC, Australia.
*Corresponding author. Email: anjana.devanand@unsw.edu.au
†Present address: CSIRO Environment, Canberra, ACT 2601, Australia.
‡Present address: CSIRO Environment, Hobart, TAS, Australia.

(*13*). We name the 2017–2019 drought the "Tinderbox Drought," in recognition of the exceptional dryness of the event and how it preconditioned the region for unprecedented fire activity.

Some aspects of the development of the Tinderbox Drought were unexpected, raising urgent questions around why southeast Australia was in drought and how human-caused climate change might be increasing drought risk and/or altering drought predictability. Here, we carry out a multidisciplinary assessment of the Tinderbox Drought to describe its characteristics, probability, drivers, and predictability. We use a broad range of observational sources, from in situ measurements to global satellite-based products, as well as different modeling and machine learning approaches to illuminate key aspects of the Tinderbox Drought. We begin with a comprehensive description of the spatiotemporal characteristics of the drought, including impacts on hydrology, vegetation and agriculture. We then assess how unusual the drought was in the context of observational data, followed by an exploration of the physical mechanisms that led to the extreme and sustained precipitation deficits. Finally, we assess the predictability of the drought and how unusual the drought was in the context of simulated long-term climate variability and what role climate change may have played in exacerbating it. We conclude by drawing together the multifaceted analysis of the Tinderbox Drought, and the insights this event gives for droughts in a warming world.

RESULTS

Characterization and impacts of the drought

We begin by identifying the temporal and spatial characteristics of the Tinderbox Drought. Droughts commonly start as a precipitation deficit (meteorological drought), which propagates to other components of the surface water cycle including streamflow and water storages (hydrological drought), soil moisture, and plant water stress (agricultural and ecological drought). While deficits in precipitation are an obvious driver of droughts, the development and intensification of droughts are also influenced by temperature, radiation, wind, and humidity that alter atmospheric evaporative demand. For example, the increased presence of high-pressure weather systems (anticyclones) during droughts in southeast Australia reduces cloud cover, increasing the local incoming radiation. These changes affect land-atmosphere feedbacks, reducing rainfall recycling in some regions, which can intensify precipitation deficits (*19*, *20*). Furthermore, soil moisture deficits reduce evaporative cooling, increasing air temperatures through increased sensible heating, increasing evaporative demand, and thereby further depleting soil moisture via a positive feedback loop.

Here, we use drought metrics (see Materials and Methods) based on precipitation, potential evapotranspiration (PET), and soil moisture to identify the focus region of the Tinderbox Drought. The impact of the drought in this region is then characterized by examining water, atmospheric, vegetation, and agricultural datasets.

The drought focus region

The Australian Bureau of Meteorology (BoM) describes precipitation deficits during the 2017–2019 drought as primarily occurring during the cool season months of April to September (*11*). Focusing on the cool season months and using a combination of drought metrics (SPI-3 and SPEI-3, see Materials and Methods) from multiple datasets, we calculate the spatial pattern of time spent in drought during the Tinderbox Drought (Fig. 1 and fig. S1A). Areas of southeast Australia

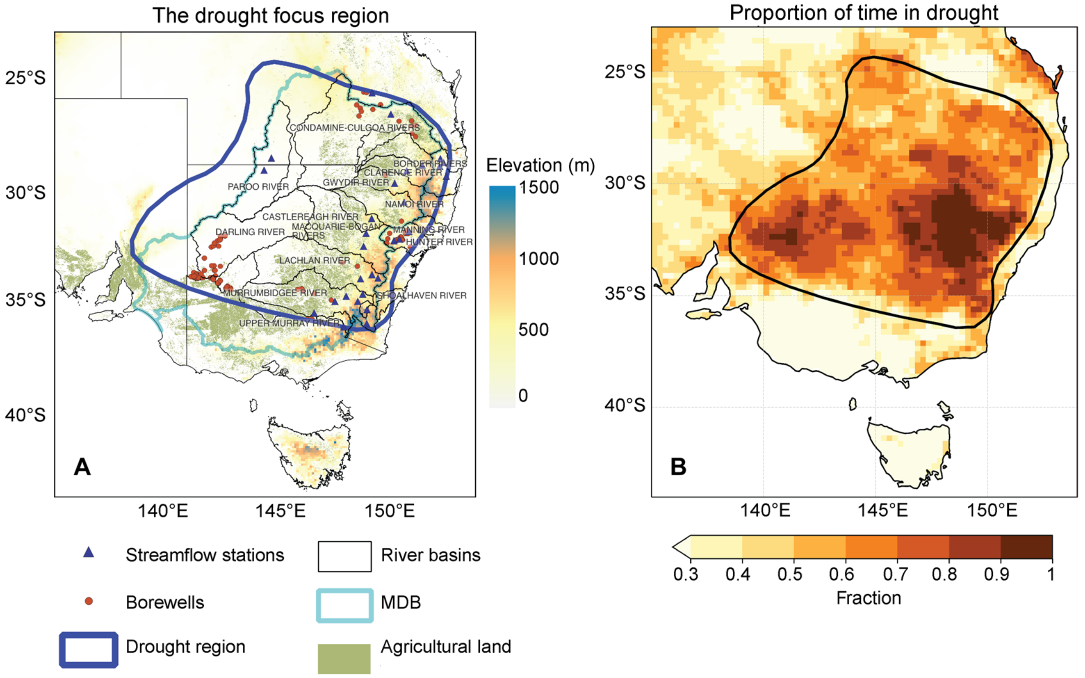

Fig. 1. The drought focus region. (**A**) The thick blue line shows the outline of the region in drought during 2017–2019. Basemap colors denote elevation. The map also shows agricultural areas, the Murray Darling Basin (MDB, thin aqua line), smaller river basins, locations of streamflow stations, and borewells. (**B**) The proportion of time in drought during April to September 2017–2019 based on standardized drought metrics. The thick black line denotes the drought area. The fraction of time spent in drought is calculated here as the mean proportion of time SPI-3/SPEI-3 ≤ −1 for data encompassing only the cool season months (April to September) of 2017–2019 based on three precipitation and two potential evapotranspiration (PET) datasets (Materials and Methods; fig. S1).

between 25° and 35°S, and east of 137°E were commonly (>50% of the time) in drought during the cool seasons of 2017–2019. Consistent results are found when repeating this analysis using all months of 2017–2019 (fig. S1B). The identified drought region is further consistent if simple rainfall thresholds (fig. S1, C and D) or a threshold approach based on root zone soil moisture data (fig. S1, E and F) is used.

We therefore define the Tinderbox Drought region (Fig. 1) based on these consistent spatial patterns of the proportion of time in drought derived from different assessment methods (fig. S1). The boundaries of the Tinderbox Drought region show a strong correspondence with the Murray-Darling Basin (MDB). The drought affected virtually all of the New South Wales (NSW) and southern Queensland parts of this major drainage basin and the agricultural land it supports (Fig. 1A). Sustained cool season drought over the full 2017–2019 interval was not evident along the coastal fringe of eastern Australia or the majority of Victoria, although some of these regions did experience drought impacts during some parts of the Tinderbox Drought. This is particularly true for the final year of the drought (2019) when most of southeast Australia experienced exceptionally dry conditions that were sustained throughout almost the full year (figs. S2 and S3), including the forested coastal and mountain regions of southeast Australia where the subsequent Black Summer fires were concentrated. The region defined here for the Tinderbox Drought (Fig. 1) is used throughout this study.

Tinderbox Drought rainfall deficits in a historical context

The Tinderbox Drought was the most intense 3-year drought experienced in our study region since Australia's gridded observational record began in 1900 (Fig. 2). It was the most severe 3-year deficit in April to September rainfall, with 2017, 2018, and 2019 all experiencing cool season rainfall that was below the 10th decile based on all years since 1900 (Fig. 2A). Previous years that experienced such intense rainfall deficits have generally been single-year events followed by median to high rainfall years. Other multi-year events with below median rainfall, such as the 3-year 1927–1929 drought event, did not have the same sustained intensity as the Tinderbox Drought.

The accumulated 3-year rainfall anomalies by the end of the Tinderbox Drought were also the most severe in the historical record of rainfall over our drought focus region (Fig. 2B). These accumulated anomalies are based on rainfall in all months. They demonstrate that the extreme April to September rainfall deficits during the Tinderbox Drought were not abated by rainfall in the intervening October–March months.

Sustained and intensifying rainfall deficits during 2017 resulted in the majority of NSW moving into drought watch conditions from mid-2017, and by October of 2017, drought conditions had become established in some regions (*21*). In some locations, the drought also involved rapid intensification as a flash drought (*22*). The intense rainfall deficits of the Tinderbox Drought form part of a multidecadal drying trend over southeast Australia (*23*). In the two decades leading to the Tinderbox Drought (2000–2019), 15 of the 20 years experienced rainfall below the long-term average (*13*). Wet years have become less frequent and generally less intense since 2000 compared to the last century, and average rainfall has been around 10% lower than the last century (1900–1999) (*24*).

Temporal evolution of the water cycle during the drought

The Tinderbox Drought affected all aspects of the water cycle. The meteorological drought conditions shown in Fig. 2 resulted from precipitation being below average for 31 out of 36 months in 2017–2019 (relative to a 1980–2016 baseline to allow for comparison across a range of different hydroclimate measures, Fig. 3A). Rainfall deficits during the cool seasons of these 3 years were about −50% (ranging from −46 to −56%). Summer precipitation was also substantially reduced, with deficits of −27% in 2016/2017, −26% in 2017/2018, and −54% in 2018/2019. Evapotranspiration (ET) deficits intensified as the multi-year drought progressed, reaching −57% by the end of 2019 (Fig. 3A). Using P minus ET (P − ET) as a measure of water

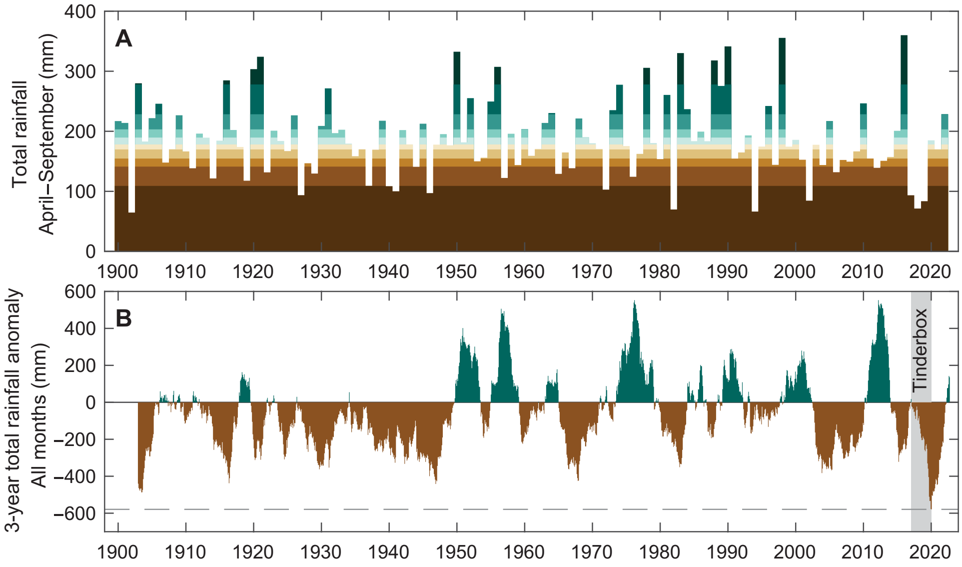

Fig. 2. Historical context for the Tinderbox Drought. (**A**) Total April to September rainfall over the drought focus region using the Australian Gridded Climate Data (AGCD) historical rainfall dataset. Shading indicates the decile over the full record length (1900–2022), where darkest brown indicates rainfall in the lowest 10% of all years and darkest green indicates rainfall in the highest 10% of all years. (**B**) Moving 3-year accumulated rainfall anomalies, relative to the 1961–1990 mean. Accumulated anomalies are based on all months and are plotted for the final month of each 3-year interval. Gray shading indicates the 2017–2019 Tinderbox Drought interval, and dashed horizontal line indicates the maximum 3-year accumulated rainfall anomaly at the end of the Tinderbox Drought.

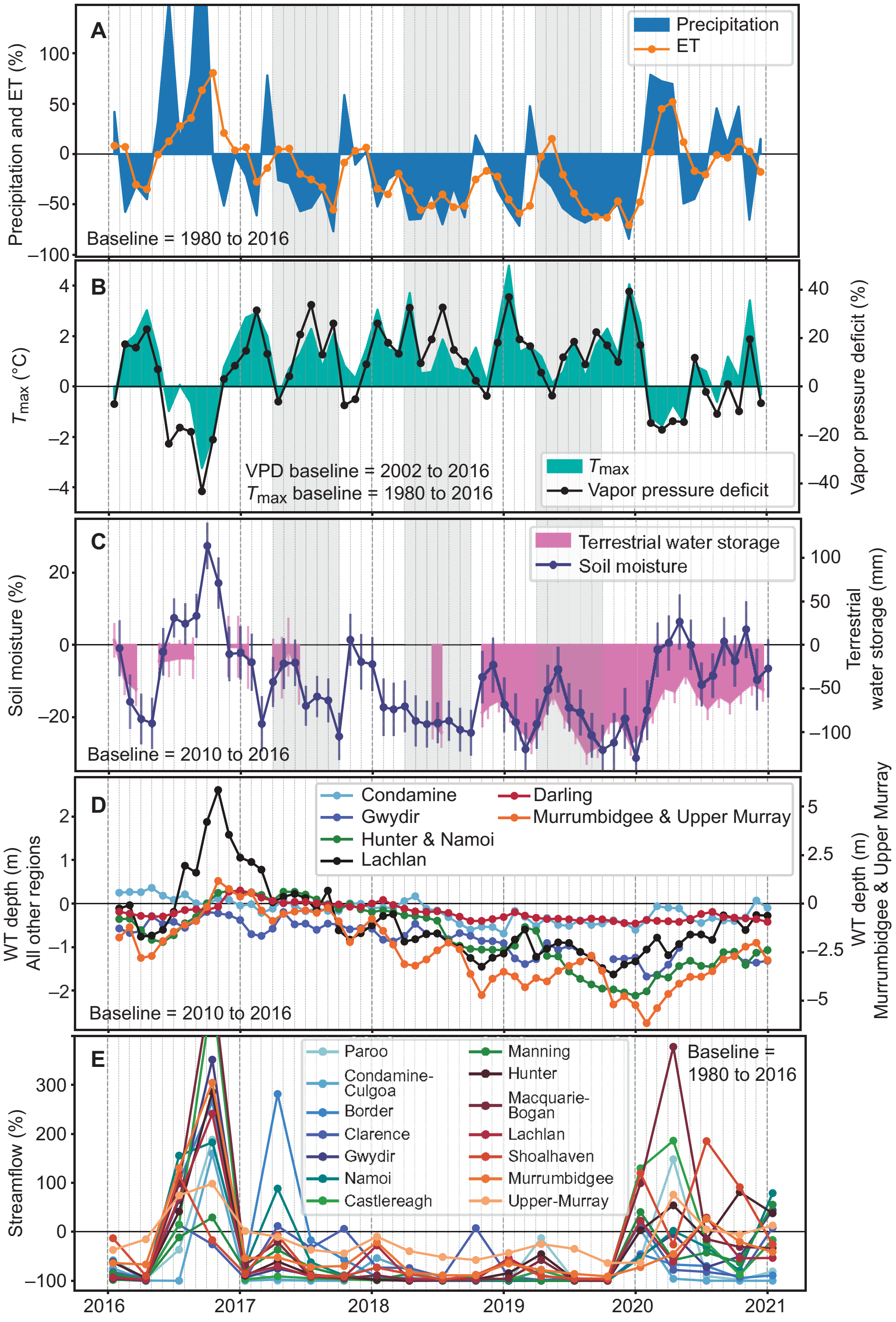

Fig. 3. Monthly anomalies in water cycle components in the drought focus region. (**A**) Precipitation and evapotranspiration (ET) (%), (**B**) vapor pressure deficit (%), and T_{max} (°C) (**C**) soil moisture from the European Space Agency dataset (%) and terrestrial water storage from Gravity Recovery and Climate Experiment (GRACE) data (mm), with error bars indicating uncertainty estimates from the same datasets. (**D**) Monthly anomalies in water table depth (m) from borewell data. The water level anomalies in the Murrumbidgee and Upper Murray are shown on the right *y* axis. (**E**) Seasonal anomalies in streamflow (%). Anomalies are calculated with respect to a baseline (1980–2016), unless constrained by data availability. The figure shows the period covering 1 year before and after the drought (2016–2020), and vertical shading in (A) to (C) indicates the cool seasons of the Tinderbox Drought.

availability, average deficits ranging from −5 to −15 mm month^{-1} occurred during the cool seasons and summers of 2017–2019. These negative water availability anomalies contributed to strong declines in water stores and streamflow (Fig. 3, C to E).

Maximum air temperatures ($T_{\max}$) and atmospheric dryness were exceptionally high during the Tinderbox Drought, culminating in several severe heatwaves that further intensified the drought conditions and fire risk (*13*, *25*). Through the drought, there was a significant inverse relationship between monthly precipitation and $T_{\max}$ anomalies (Fig. 3, A and B), with months of higher-temperature anomalies coinciding with months of greater precipitation deficits ($r = -0.39$, t test two-tailed $P < 0.05$). This monthly covariance between temperature and precipitation anomalies is also a robust feature of the longer-term interannual climate variability of this region (*13*). $T_{\max}$ was on average 1.6°C higher than the 1980–2016 mean over the drought focus region, with the largest anomalies over summers (1.8 to 2.8°C) (Fig. 3B). Anthropogenic warming over the 20th century also means that the 1980–2016 baseline used here is 0.3°C above the 1911–1940 average. The exceptional heat during the Tinderbox Drought differentiates this event from previous drought events in southeast Australia that have typically been associated with temperatures around 1.0°C above the long-term mean (*11*).

Vapor pressure deficit (VPD) is a measure of the ability of the atmosphere to take up water from the surrounding landscape. VPD is determined by atmospheric temperature and humidity and is an important driver of ecological stress. Between November 2016 and January 2020, 34 of the 39 months experienced above average VPD anomalies, and over the 3 years of the Tinderbox Drought, the mean VPD anomaly was 15% greater than the 2002–2016 baseline mean (Fig. 3B). We estimate VPD anomalies here from a shorter baseline for consistency with assessments using satellite-based vegetation datasets.

Surface and groundwater datasets demonstrate the progressive worsening of hydrological drought during 2017–2019 (Fig. 3, C to E). During 2017, surface soil moisture was on average −11% relative to the predrought 2010–2016 mean. In 2018, the soil moisture anomaly intensified to −18%, and in 2019, it intensified again to −22% (Fig. 3C). By 2019, these moisture deficits amounted to around a 100-mm lowering of terrestrial water storage (TWS; below the 2010–2016 mean). Water table depths also declined progressively through the drought (Fig. 3D), with maximum lowering of −6.1 m measured for the Murrumbidgee and Upper Murray basin region in early 2020. By spring of 2019, streamflow anomalies had declined to −91 to −100% below long-term 1980–2016 levels in all river basins of our study region except the Upper Murray (−64%) where flows are less variable than other basins (Fig. 3E). Drought monitoring in NSW saw drought indicators from soil moisture and plant growth deficits appear several weeks ahead of meteorological drought indicators during both the 2017 drought onset and the drought intensification in 2019 (*13*).

The Tinderbox Drought ended with positive precipitation anomalies during February to April 2020, which were also accompanied by negative $T_{\max}$ and VPD anomalies. Soil moisture across the drought region recovered quickly in February/March 2020. Recovery of streamflow occurred variably through 2020 as rain fell across different parts of the drought-affected region. An exception was the Border and Condamine-Culgoa river basins in the northern part of the drought focus region, where negative streamflow anomalies continued to persist through to the end of 2020. Water table and TWS anomalies demonstrate a much slower recovery from the impacts of the Tinderbox Drought. Although positive water table trends were seen from early 2020, negative anomalies persisted in all basins until at least mid-2020. By the end of 2020, nearly a year after the drought-breaking rainfall that ended the meteorological drought, negative water table anomalies of about −2.9 m still remained in the Murrumbidgee and Upper Murray basin regions.

The impact of the drought on vegetation

Sustained soil moisture and VPD anomalies and the resulting impacts on vegetation were a defining feature of the Tinderbox Drought and subsequent Black Summer fires. Soil moisture droughts reduce the water supply to plants, whereas atmospheric droughts (anomalously high VPD) increase the atmospheric demand for water from the plant. Plants generally respond to increasing VPD by closing stomata (*26*), which reduces photosynthesis and transpiration. The reduction of transpiration reduces latent cooling, causing leaves to heat up and potentially exceed their photosynthetic optimum temperature. Even if plants shed leaves to reduce water loss, the lack of soil moisture and the high VPD can still lead to serious impacts (*27*). High VPD can also increase fuel dryness leading to elevated fire risk (*28*).

VPD was a key difference between the Tinderbox Drought and earlier major droughts in southeast Australia (Fig. 4, A and B). In 2016, VPD was already high over the northeastern half of the drought region, indicating the potential for ecological stress to increase before soil moisture deficits developed across the region (Fig. 4C). Positive VPD anomalies became more widespread and intense throughout the Tinderbox Drought, so that VPD was between 25 and 50% higher than average across the drought focus region by spring [September to November (SON)] of 2019 (Fig. 4B). The progressive intensification of VPD anomalies through the drought suggests a role in sustaining and intensifying the Tinderbox Drought. In contrast, the Millennium Drought in our study region only had a 10% VPD anomaly during a single year, 2002, and did not show a sustained increase in VPD through the drought event (Fig. 4A). However, we do note that the Millennium Drought was focused on the southern MDB (primarily Victoria) and did not affect the full study area assessed here for the Tinderbox Drought. Previous work has demonstrated that there has been a sustained positive trend in VPD over southeast Australia, such that during the Tinderbox Drought, the long-term VPD conditions had emerged outside of the range of historical (1950–1999) experience (*13*).

A clear progression of vegetation stress occurred during the Tinderbox Drought, which we illustrate for spring (SON) of each year (Fig. 4, C and D). Vegetation optical depth (VOD), a remote sensing proxy of plant canopy moisture content, was high in 2016 but was followed by an accumulation of increasingly negative anomalies as the Tinderbox Drought developed and intensified through to the end of 2019 (Fig. 4C). This effect can also be seen using the Normalized Difference Vegetation Index (NDVI), a long-established proxy of canopy leaf area (Fig. 4D). In 2016, there were widespread positive NDVI anomalies (i.e., higher canopy area), but this was followed by a precipitous drop in the subsequent drought years. By spring of 2019, more than 96% of the drought region experienced negative NDVI anomalies, with a mean anomaly of −22% (Fig. 4D). The spatial development of vegetation stress closely resembled the intensification of positive VPD anomalies (Fig. 4B), demonstrating how VPD exacerbated the drought's impact on vegetation. The lack

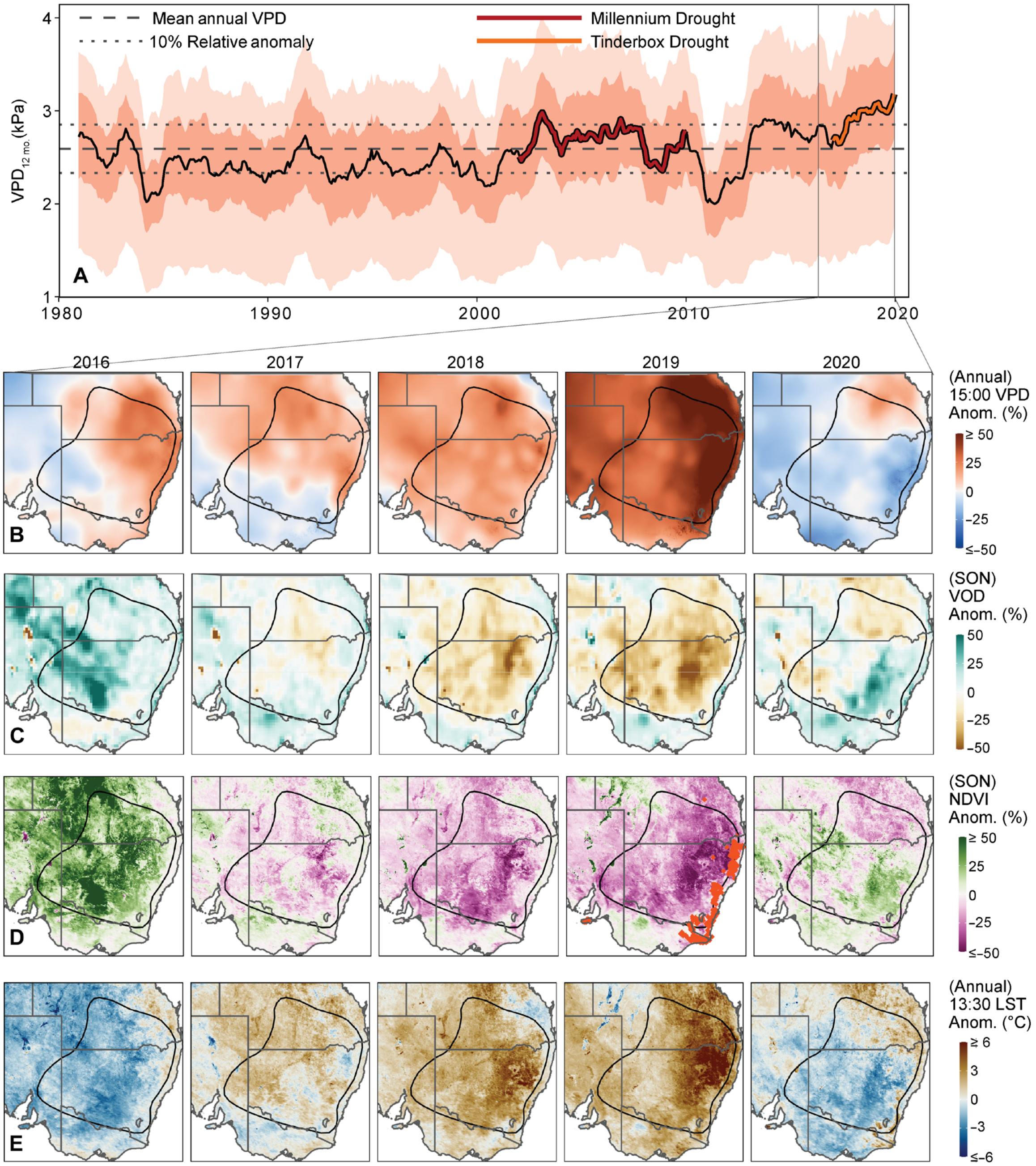

Fig. 4. The evolution of the drought impacts on vegetation in southeast Australia. (**A**) The 12-month rolling mean of vapor pressure deficit (VPD; 15:00 hours reading from AGCD) across the focal region is shown for 1981–2020. The shadings show the inner 50% and 90% range of the focal region's VPD. The mean annual VPD and 10% deviation are overlaid. The Millennium and Tinderbox droughts are highlighted. (**B**) The relative VPD anomaly expressed as a percent deviation from the 2002–2016 mean annual value. (**C**) The relative anomaly of the vegetation optical depth (VOD) during September to November (SON) is plotted as a percent deviation from the 2002–2016 SON seasonal mean. (**D**) The relative anomaly of the Normalized Difference Vegetation Index (NDVI) is plotted as a percent deviation from the 2002–2016 seasonal (SON) mean. Regions that experienced burning during the 2019 Black Summer fires are denoted by orange points. (**E**) The annual mean of the daytime (13:30 overpass time) land skin temperature anomaly (LST; °C) as derived from the MODIS AQUA platform.

of plant moisture and canopy area also reduced evaporative cooling over the drought region. This is evident via the close correspondence of the spatial distribution and intensity of NDVI and surface temperature anomalies during the Tinderbox Drought, leading to an increase of land surface temperatures as the drought progressed (Fig. 4E).

Agricultural impacts during the drought

Australia is one of the top 10 producers and exporters of wheat, barley, and cotton worldwide. Australian wheat accounts for almost 10% of global wheat trade, amounting to a 2018–2021 average export value of 5.3 billion AUD (*29*). Australian barley production accounts for 30 to 40% of the world's malting barley trade and 20 to

30% of global feed barley trade amounting to a 2017–2021 average export value of 2 billion AUD (*30*). Southeast Australia is the major center for this agricultural production, providing around 40% of the nation's total agricultural output.

The impacts of the Tinderbox Drought on wheat and barley production across the drought-affected region were considerable, especially in the second and third year of the drought (fig. S4). Wheat and barley are winter crops and predominantly rainfed, leading to high sensitivity to interannual variations in cool season rainfall. Wheat production in 2018 and 2019 dropped by 73% and 63%, and barley production dropped by 47% and 43% compared to the 1990–2016 average. Wheat showed negative yield anomalies in all 3 years of the drought. Within the observation period for which yields at the sub-national scale are available (starting in 1990), negative yield anomalies over three or more years have only been seen previously during the Millennium Drought (in 2002–2004 and 2006–2009). Similarly, barley exhibited negative yields in two consecutive years (2018 and 2019), which had only been observed once before in 2006–2007 of the Millennium Drought.

Agricultural production data for rice and cotton are only available at a national scale; however, the major production areas for these crops occur within the focus region of the Tinderbox Drought. Rice and cotton are irrigated summer crops with a growing season ranging from spring to autumn, and are particularly vulnerable to reduced availability of irrigation water. Rice was the most negatively affected of all four assessed crops, with reductions in rice production of more than 90% in the 2018/2019 and 2019/2020 growing seasons, compared to the long-term 1990–2016 average (fig. S4C). These production losses were driven by strong decreases in the area harvested, which was reduced by 92 to 95% in 2018/2019 and 2019/2020. The area used for cotton in 2018–2019 dropped to 10% below the long-term average, and production reduced to a +12% anomaly, down from +71% in the previous year. Severe decreases in cotton production were then seen in the 2019/2020 growing season when cotton production dropped to −74% compared to the 1990–2016 average, the lowest value since 1982/1983. This drop was driven by a strong reduction in the harvested area to −79% compared with the long-term mean.

The production data underline the severity of the Tinderbox Drought for agricultural producers in southeast Australia. The impacts of meteorological drought appear to be particularly evident for wheat and barley production, which were affected by deficits in cool season rainfall particularly in 2018 and 2019 (Fig. 3A and fig. S4, A and B). Because rice and cotton are irrigated crops, their production is strongly linked to access to irrigation water and fluctuations in water markets. These irrigated crops appear to have been affected primarily by the intensification of hydrological drought as the Tinderbox Drought progressed, causing extreme water table and streamflow deficits by 2019 (Fig. 3, D and E, and fig. S4, C and D).

Probability of drought occurrence

The Tinderbox Drought involved extreme and sustained precipitation deficits, but how unusual were these in the context of natural climate variability? It is well established that the short length of the observational rainfall record in southeast Australia is insufficient to capture the full possible range of natural hydroclimatic variability (*31*–*33*). However, existing paleoclimate proxy-based assessments of long-term Australian rainfall variability were developed for specific regions that do not match the region used consistently throughout this study. Therefore, to address this limitation and test how unusual the three sequential years of 2017–2019 were, we use two complementary approaches. First, we assess randomly resampled 3-year anomalies of cool season rainfall using the 1900–2019 observed rainfall data for the drought focus region. Second, we use linear inverse models (LIMs) as an empirically based null hypothesis for the observed precipitation deficits occurring due to internal climate variability (Materials and Methods; Fig. 5).

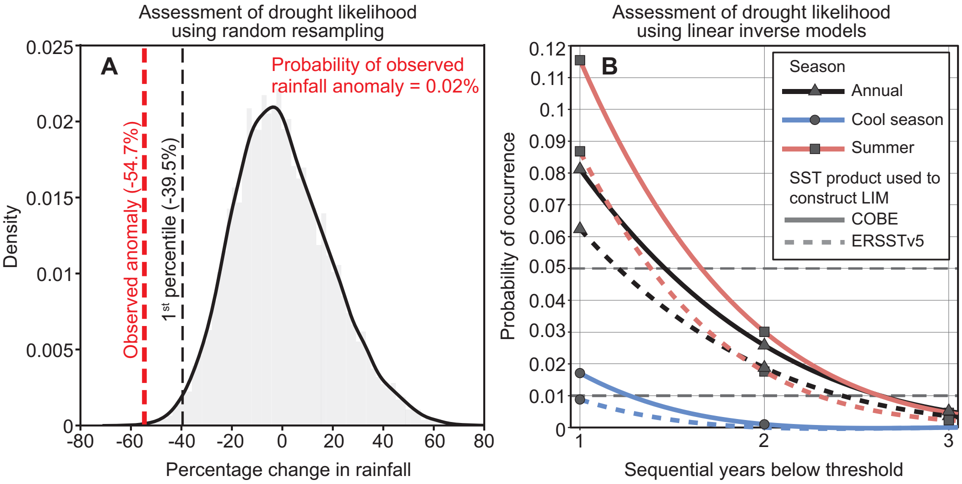

Fig. 5. Probability that the 2017–2019 southeastern Australian meteorological drought occurred within the range of internal variability. (**A**) The observed deficit in cool season (April to September, AMJJAS) rainfall of the Tinderbox Drought (2017–2019; red dashed line) relative to the first 60 years of the observational period (1900–1959). The likelihood of the observed 2017–2019 rainfall deficit is assessed relative to random resampling of the full historical period (1900–2019) 10,000 times and computing the precipitation anomaly of the last 3 years compared to the first 60 years of the resampled data (gray shaded distribution). The black dashed line indicates the 1% significance level based on the bootstrapping relative frequency distribution. (**B**) Probability of occurrence of the least severe annual (black), cool season (AMJJAS; blue), and summer (December to February, DJF; salmon) precipitation deficit observed during the 2017–2019 drought, for one, two, and three sequential years as estimated from the LIMs. The solid line shows the distribution constructed using SST data from COBE, and the dotted line shows the distribution constructed using SST from ERSSTv5. Dashed horizontal gray lines show 5% and 1% significance levels.

The likelihood of 3-year cool season rainfall deficits equivalent to what occurred during the Tinderbox Drought is exceptionally low (Fig. 5A). Random resampling of individual years (with replacement) from the full observational rainfall record for the drought region demonstrates that the observed Tinderbox Drought anomalies were at the 0.02% level of 10,000 random rearrangements of the historical record. This suggests that the likelihood of the observed 2017–2019 cool season rainfall deficits happening due only to natural climate variability was exceptionally low.

The precipitation deficits of the Tinderbox Drought were also exceptionally unlikely when assessed against an empirically based null hypothesis (Fig. 5B). Unlike the random resampling of observed precipitation (Fig. 5A), the LIM precipitation trajectories maintain temporal autocorrelations (Materials and Methods). This allows assessment of the temporal evolution of the drought, and how unusual this was in the context of mostly ocean-forced internal climate variability. The probability of experiencing a single-year cool season precipitation deficit equal to that of 2017—the least severe year of the Tinderbox Drought—was between 0.9 and 2%. The full annual precipitation deficit for 2017 had a likelihood of 6 to 8%. Expanding the assessment to examine sequential precipitation deficits at least as severe as 2017 demonstrates an increasingly low likelihood (Fig. 5B). Three sequential years of cool season deficits at least as severe as 2017 are outside the range of simulated variability, occurring at a rate of 0% in the LIM simulations. The observed Tinderbox Drought was even more severe than this, given 2017 had the least dry cool season of the three drought years. Three sequential years of annual and summer deficits at least as severe as the least dry year of the drought are also extremely unusual (<1%) within the range of internal precipitation variability.

Together, these assessments indicate that the likelihood of experiencing a meteorological drought as severe as the 2017–2019 event is much less than 1%, if we assume that the event and the historical record were wholly driven by internal climate variability. This means that the Tinderbox Drought was either an exceptionally rare natural event, or that anthropogenic forcing played a role in exacerbating this drought.

Mechanisms driving the drought

Large-scale climate drivers

Australia's highly variable rainfall is frequently linked to large-scale modes of climate variability. Dry conditions in southeast Australia are commonly associated with El Niño or positive Indian Ocean Dipole (IOD) events, while the Southern Annular Mode (SAM) causes differing rainfall impacts between the cool and warm seasons. The state of these modes of variability contribute to long-range (seasonal) rainfall outlooks, and previous major multi-year droughts in southeast Australia have been linked to these drivers. For example, the Federation Drought (1895–1902) has been linked to high El Niño activity and a positive phase of the Interdecadal Pacific Oscillation (*34*), while the World War II Drought (1937–1945) has been related to cool sea surface temperatures (SSTs) in the eastern Indian Ocean (*34*). The Millennium Drought (or Big Dry, 1997–2009) was influenced by a positive SAM phase, and a series of Central Pacific El Niño events (*34*, *35*). Recent work has also highlighted the importance of the rain-promoting phases of the modes of variability—specifically La Niña and negative IOD events—in ending droughts over southeast Australia (*36*–*38*).

Large-scale ocean variability played some role in driving rainfall deficits during the Tinderbox Drought, although with notable differences to the large-scale modes of variability that have commonly been used to assess the drivers of past droughts. Interannual rainfall variability during April to September in the Tinderbox Drought region is significantly correlated with SST in the tropical oceans around northern Australia (Fig. 6, A and C; $r = 0.77$ for the region 5° to 20°S, 100° to 160°E), with the highest correlations observed in the eastern Indian Ocean and Coral Sea sectors (Fig. 6A). This confirms previous studies that have identified the importance of ocean temperatures to the north of Australia for rainfall in the southeast of the country (*39*–*41*). The correlation strength between the ocean north of Australia and cool season rainfall anomalies over the drought region surpasses those from the traditional El Niño Southern Oscillation (ENSO) indices commonly used to inform seasonal outlooks of rainfall, i.e., Niño3.4 index ($r = -0.52$; Fig. 6E), Niño4 index ($r = -0.54$; Fig. 6D), and the Southern Oscillation Index ($r = 0.58$).

ENSO was neutral in April to September of 2017, developed into a weak and short-lived La Niña by the end of 2017, and returned to neutral conditions by mid-2018 (Fig. 6F). The sign and strength of the tropical Pacific SST suggest that ENSO was unlikely to have promoted the large rainfall anomalies in southeast Australia at the start and intensification of the drought. A weak Central Pacific El Niño developed in late 2018 and persisted through winter 2019 (Fig. 6F, blue line), and has been suggested to have contributed to the cool season rainfall deficits of the final year of the Tinderbox Drought (*42*) and into the Black Summer of 2019/2020. However, the absence of sustained and/or strong El Niño conditions during the Tinderbox Drought suggests that ENSO was not a major driver for this drought, despite the longer-term importance of tropical Pacific climate variability for rainfall in eastern Australia in both the cool and warm seasons (Fig. 6, D and E, and fig. S5).

The IOD was weakly positive in April to September of 2017 and 2018, and a record positive IOD event occurred in 2019 (Fig. 6F), promoting below-average winter-spring rainfall in southeast Australia (*13*). The relationship with the Dipole Mode Index (DMI) and cool season rainfall in our study region ($r = -0.61$) is dominated by SST anomalies in the eastern pole used for the DMI ($r = 0.69$, Fig. 6, A and B). SSTs in the eastern IOD region were consistently below their climatological mean for all 3 years of the Tinderbox Drought. Previous studies have also pointed to the eastern pole of the IOD being the element that is important for Australian rainfall variability (*40*). Cool SST anomalies in the eastern Indian Ocean (and the absence of warm SST anomalies from negative IOD events) have also been suggested to be more important than tropical Pacific Ocean conditions in establishing and sustaining previous major droughts in southeast Australia (*36*). Our findings suggest that the importance of eastern Indian Ocean SST anomalies also held true for the Tinderbox Drought.

The 3 years of the Tinderbox Drought were characterized by cool SST anomalies across widespread areas in the eastern Indian Ocean and Southern Ocean (fig. S6). These cool SST anomalies continued to intensify and spread further east from 2017 to 2019, such that by April to September of 2019, almost all of the ocean area around Australia was below average. The exception to this was the warm SST anomalies that persisted off eastern Australia, adjacent to the drought region. The synoptic processes that help explain the observed connections between remote SST anomalies, moisture transport, and rainfall anomalies during the Tinderbox Drought are investigated in the subsequent sections.

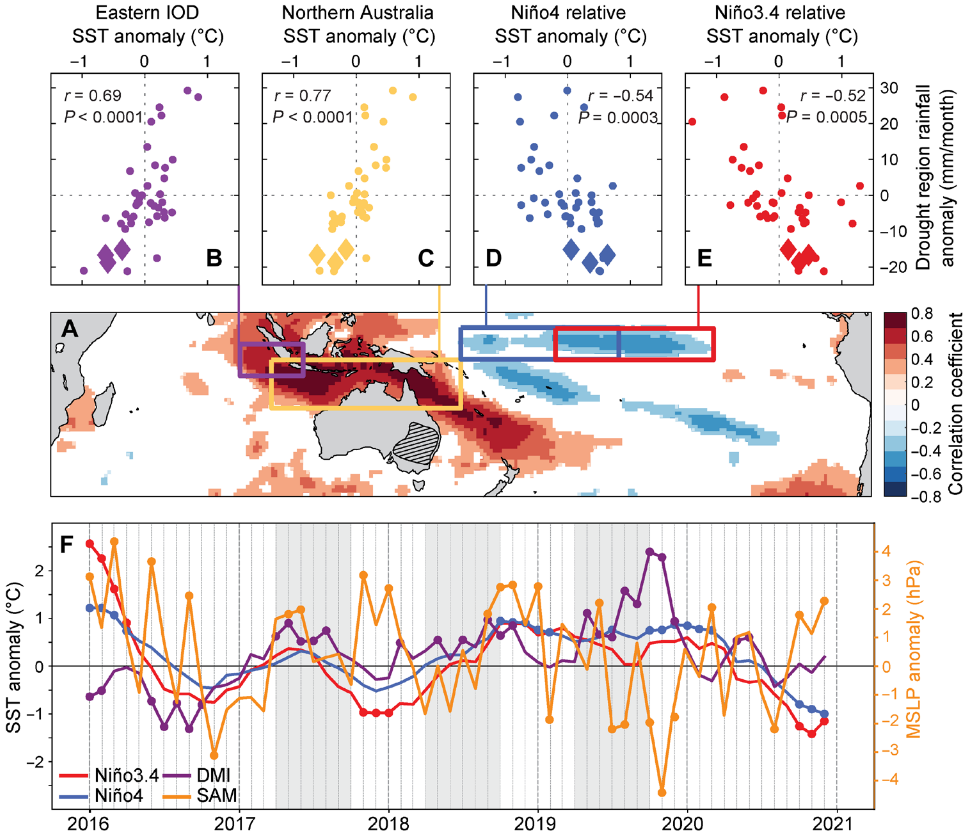

Fig. 6. Sea surface temperature and large-scale influences on rainfall in the Tinderbox Drought region. (**A**) Spatial correlation of April to September rainfall anomalies in our study region (hatching) with SST anomalies, showing only correlations significant at $P < 0.1$. Colored boxes show the southeast tropical Indian Ocean (purple, 0 to 10°S and 90° to 110°E), northern Australia (orange, 5° to 20°S and 100° to 160°E), Niño4 (blue, 5°N to 5°S and 160°E to 150°W), and Niño3.4 (red, 5°N to 5°S and 120° to 170°W) regions explored further in (B) to (E). (**B** to **E**) Relationship between rainfall anomalies in our study region with SST averaged over regions indicated in (A), for April to September anomalies between 1982 and 2020 (circles), with the 2017–2019 Tinderbox Drought years indicated by diamonds. Data in this figure use the OISST v2 0.25° × 0.25° SST product and the ACGD rainfall product (Materials and Methods). All data in (A) to (E) are linearly detrended to isolate interannual variability and the Niño3.4 relative index (D) is calculated by first removing the tropical ocean mean (*83*). Anomalies in (B) to (E) are relative to 1982–2016 climatology (Methods). (**F**) Time series of the Niño3.4 (red), Niño4 (blue), DMI (purple), and SAM (orange) indices between 2016 and 2020. Months that exceed 1 SD of the respective index (computed over 1980–2016) are indicated with markers. Gray shading denotes the cool seasons of the Tinderbox Drought.

In addition to tropical climate drivers and their associated SST anomalies, rainfall variability in southeast Australia is also influenced by atmospheric variability of the SAM. The positive phase of the SAM (poleward shift of the mid-latitude jet) is associated with decreased rainfall over parts of southern and eastern Australia during the cool season (*43*). However, no significant relationship is evident in the correlation of the cool season SAM with rainfall anomalies averaged across our study region ($r = -0.05$, $P = 0.69$, 1958–2022), possibly owing to opposing rainfall effects of the SAM in the northern and southern parts of the drought region (*13*). The SAM was mostly neutral throughout the 2017–2019 drought and switched regularly between its positive and negative phases (Fig. 6F). An exception to this was the strong and sustained negative SAM that developed following a Sudden Stratospheric Warming event over Antarctica in the spring of 2019. This event likely exacerbated drying and increased bushfire risk toward the end of the Tinderbox Drought (*13*, *44*).

Moisture sources

Although there is a significant connection between distant climate drivers and SST anomalies to precipitation over the Tinderbox Drought region, the actual sources of moisture for this region are generally more local. The primary source of moisture contributing to southeast Australia's rainfall comes from the Coral and Tasman Seas, immediately to the east of Australia (*20*). Here, we use the Lagrangian model named FLEXPART to understand how moisture sources varied during the drought event (see Materials and Methods for further details). The Lagrangian model estimates that, on average, 95% of moisture supplied to the Tinderbox Drought region comes from local sources near eastern Australia, extending to the Tasman and Coral Seas [(*20*); fig. S7]. About 30% (71.4 mm) of these moisture sources occur during the cool season from April to September, i.e., the time of the year when rainfall was consistently low during the Tinderbox Drought. Of those cool season moisture sources, 65.7% are from the nearby ocean, while 34.3% come from the land.

Analysis of moisture source regions suggests that the Tinderbox Drought was initiated and sustained by a decline in oceanic moisture supply to the drought region in 2017–2019, and exacerbated in 2018 and 2019 by reduced moisture supply from terrestrial sources. Our analysis indicates that in the 2017 cool season (April to July) the moisture supplied by the oceanic sources was 16% weaker than usual (Fig. 7A and fig. S8A). The decline in oceanic moisture supply to the region intensified in the cool season of the following year (Fig. 7B), worsening the drought in 2018 (28% lower). In 2019, the oceanic moisture contribution was on average only slightly lower than usual (5% lower). This was characterized by increased oceanic-sourced moisture in the western part of the drought region that partly offset continued negative anomalies from oceanic sources in the eastern part of the Tinderbox Drought region (Fig. 7C). Additionally, the cumulative rainfall deficit over the Tinderbox Drought region also led to anomalously low moisture contribution from terrestrial sources in 2018 and 2019 (Fig. 7, E and F; 25% less moisture in 2018, and 27% less in 2019), which exacerbated the severity of the drought.

SSTs in the Coral and Tasman Seas were warmer than usual during much of the Tinderbox Drought, which might have been expected to increase oceanic moisture to the drought region (fig. S6). Warm SSTs combined with increased wind speed (Fig. 7, G to I) and below normal specific humidity (fig. S8, G to I) did indeed promote evaporation (fig. S8, D to F) from the main oceanic source regions. However, anomalous anticyclonic circulation (Fig. 7, G to I) transported moisture away from the Tinderbox Drought region toward the northern parts of Australia and the Maritime Continent. This is evidenced by the positive oceanic moisture sink anomalies over Queensland in 2017–2018 and extending over the Northern Territory in 2019 (Fig. 7, A to C).

Synoptic factors

Reductions in seasonal-scale rainfall during the Tinderbox Drought were partly connected to remote SST anomalies and transport of oceanic-sources moisture, but were ultimately the result of changes to synoptic scale weather systems on daily time scales. Rain-bearing weather systems reduced in frequency and produced less rainfall during the drought.

Rainfall deficits during past droughts in southeast Australia have, in previous studies, been associated with changes in the frequency of rain-bearing weather systems (*45*, *46*) and the amount of rainfall falling per system (*45*). In particular, the absence of weather systems that bring heavy rainfall, equivalent to around the 95th percentile or higher of daily rainfall amounts, are the dominant cause of rainfall deficits during drought in southeast Australia (*47*). The reduction or absence of heavy rain-bearing weather systems can be influenced by large-scale modes of climate variability, stochastic changes to weather regimes, or combinations of both (*48*, *49*). Concurrently, the frequency and intensity of weather systems that limit rainfall over southeast Australia increase during drought, with an increased occurrence and intensity of synoptic-scale anticyclones (that form the quasi-stationary subtropical ridge) during past multiyear drought periods (*50*).

During the Tinderbox Drought, there was a shift toward lower daily rainfall totals across the distribution of daily rainfall data from 2017 to 2019, compared with a 1980–2016 climatology. These distributions were computed using rain days only, which were defined as days above 0.01 mm/day, at each grid point within the drought region (Materials and Methods). However, the nature of rainfall also changed, with a relatively larger decline in heavy rainfall days (Fig. 8A). The Tinderbox Drought region typically receives half or more of its seasonal rainfall from "heavy rain days" where the rainfall totals are above the climatological 90th percentile of rain days from 1980 to 2016. Seasonally, December to February (DJF), March to May (MAM), June to August (JJA), and SON receive a median of 63, 59, 51, and 51%, respectively, of their seasonal rainfall accumulations from these heavy

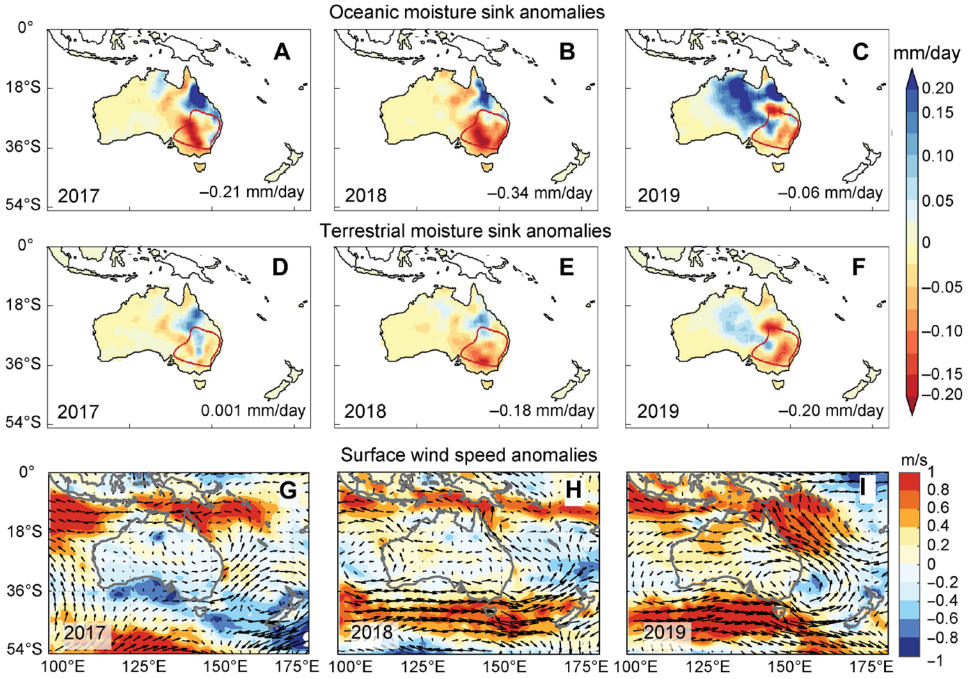

Fig. 7. Sources of moisture during the Tinderbox Drought. Anomalies of (**A** to **C**) oceanic moisture sink (mm/day), (**D** to **F**) terrestrial moisture sink (mm/day), and (**G** to **I**) 850 hPa winds (m/s, vectors) and wind speed (m/s, shading). Anomalies are calculated relative to April to July 1980–2016 climatology from April to July for [(A), (D), and (G)] 2017, [(B), (E), and (H)] 2018, and [(C), (F), and (I)] 2019 relative to April to July 1980–2016 climatology. Note that the analysis uses a shorter cool season (April to July) due to ERA-Interim data availability (stops in August 2019). April to September moisture source and sink anomalies for 2017 and 2018 can be seen in fig. S9.

rain days. That is, half or more of the seasonal accumulation occurs on just 10% of the days when it rains.

Despite the overall reduction in rainfall from all rain days during the Tinderbox Drought, the relative contribution from heavy rainfall to the seasonal accumulation decreased considerably more than non-heavy rainfall (i.e., rain days <90th percentile). The relative contribution of heavy rain days to seasonal totals was lower than normal during all seasons from DJF 2016/2017 to DJF 2019/2020 with the exception of MAM 2019, with median reductions ranging from +3 to −49% (Fig. 8A). Median changes to non-heavy rain days ranged from −3 to +49%, as expected. The largest reductions in heavy rain days were during winter (JJA), when the contribution of heavy rainfall to the seasonal total decreased by 26%, 39%, and 49% in 2017, 2018, and 2019, respectively. Given the climatological contribution of heavy rainfall days is 51% for JJA, this shows that there were very few, if any, heavy rain days during the Tinderbox Drought winters. An analysis at the gridbox scale shows that there were no heavy rain days during some winters in some parts of the domain.

The changes to daily rainfall described above can be associated with different types of synoptic weather systems. Six weather objects [i.e., anticyclones, cyclones, fronts, warm conveyor belts, and potential vorticity (PV) streamers and cutoff lows] were examined during the winters (JJA) of the Tinderbox Drought when rainfall reductions were most pronounced. Daily rainfall data were then attributed to each object (Materials and Methods). Throughout the three winters of the Tinderbox Drought, the intensity and frequency of rainfall decreased for every type of weather object examined here (Fig. 8, B to E). The largest declines were mainly associated with warm conveyor belts and PV streamers. In the winter of 2017, the total rainfall reduction was due to decreased frequencies of rainfall from each type of weather system, with frequency changes for all objects ranked in the lowest 10 years of the 40-year record (Fig. 8C). Decreases in the intensity of weather-associated rainfall were more important during the winters of 2018 and 2019 (Fig. 8, D and E). In 2019, the rainfall frequency reductions related to cyclones, warm conveyor belt inflows, and ascents were the second lowest in the 40-year record, and fronts were the third lowest on record. Similarly, the rainfall intensity reductions related to cyclones, warm conveyor belts, and cutoffs were the third or second lowest on record, while the rainfall intensity reductions related to PV streamers were the lowest on record (Fig. 8E).

These results suggest that Rossby wave breaking and warm conveyor belts occurred less often in the winter of 2017, and produced less intense rainfall over the domain in the following two winters. The reduced rainfall associated with warm conveyor belts was likely due to reduced moisture at the inflow level of warm conveyor belts and/or weaker ascending air in warm conveyor belts as a result of weakened upward motion forced by the upper-level wave breaking (*51*). In combination with the results from the analyses of moisture sources, it appears that reduced moisture inflow to warm conveyor belts is likely to have been a major source of the synoptic-scale rainfall reduction during the Tinderbox Drought.

Land-atmosphere feedbacks during the drought

Sustained water deficits during droughts can feedback through land-atmosphere coupling to intensify atmospheric heating, and it is notable that the final year of the Tinderbox Drought was Australia's driest and hottest year on record, both in southeast Australia and nationwide (*13*). We examined the impact of soil moisture drought on summer temperatures using the WRF model by contrasting simulations where soil moisture was varied to reflect drought and climatological conditions (Materials and Methods).

The simulated soil water stress experienced by vegetation increased by 10 to 50% during the Tinderbox Drought relative to climatological conditions across southeast Australia (fig. S10, A and F), leading to a decline of 5 to 60 W m^{-2} in the latent heat flux (fig. S10, B and G) and a consequential increase in the sensible heat flux (fig. S10, C and H) across widespread areas. As a result, the drier soil moisture increased the summer-mean daily maximum temperature by ~0.25° to 1.5°C (fig. S10, D and I) and decreased air humidity by 2 to 16% from the east coast extending to ~400 km inland. During heatwave periods (e.g., 14 to 26 January 2019 and 16 December 2019 to 7 January 2020), the soil moisture drought exerted an increasingly strong constraint on transpiration (fig. S10, K and P). Overall, the drought conditions and the consequential changes in sensible and latent heat fluxes amplified heatwaves by up to 2.5°C, as well as tended to dry the lower atmosphere. These changes, in turn, are likely to have led to further drying and the elevated fire risk that culminated in the Black Summer fire disaster.

Predictability of the drought

The development of the Tinderbox Drought in mid-2017 occurred during a time when more normal rainfall conditions were expected in southeast Australia (*52*). Neutral states of the ENSO and mild positive IOD anomalies during 2017 and 2018 winters (Fig. 6F) meant that traditional indicators (e.g., Niño3.4 and DMI) that often guide public discourse around heightened drought risk were not prominent. As shown in our earlier analysis (Fig. 6), these traditional indicators may not provide an optimal representation of the large-scale drivers of drought risk in our study region. Other aspects of the drought, including the development of soil and agricultural drought indicators ahead of meteorological indicators, and the heightened temperature and high VPD conditions in which this drought formed compared with previous droughts, all point to the challenging and changing conditions that may have affected predictability of the Tinderbox Drought. Here, we apply prediction methods that have been developed in prior work to understand drought likelihood (*53*) and drought-breaking probabilities (*54*) to the Tinderbox Drought (Materials and Methods).

Machine learning–based insights into predictability

Machine learning may offer insights into the predictability of drought, particularly given the multitude of factors that together resulted in the Tinderbox Drought. Here, we apply the explainable machine learning method used by Hobeichi *et al.* (*53*) to the Tinderbox Drought. This method initially constructs a damage function with Random Forest (RF) to model the relationship between observed drought impacts and concurrent climate conditions. The set of climate predictors encompasses large-scale modes of variability and local-scale climate variables (see Materials and Methods), ensuring high accuracy in identifying drought events (fig. S11B). The trained RF yields scores indicating the importance of each predictor in the model. Additionally, it can predict the probability of drought occurrence based on the prevailing climate conditions (fig. S11C).

Concentrating on 2019 (due to data availability, see Materials and Methods), the feature importance analysis indicates that ENSO was not a dominant driver of the drought in 2019 (fig. S12). This is despite Australian droughts overall being sensitive to large-scale climate drivers, and ENSO in particular, as shown by an analysis of all drought events that have occurred since 2000 (fig. S12, blue bars).

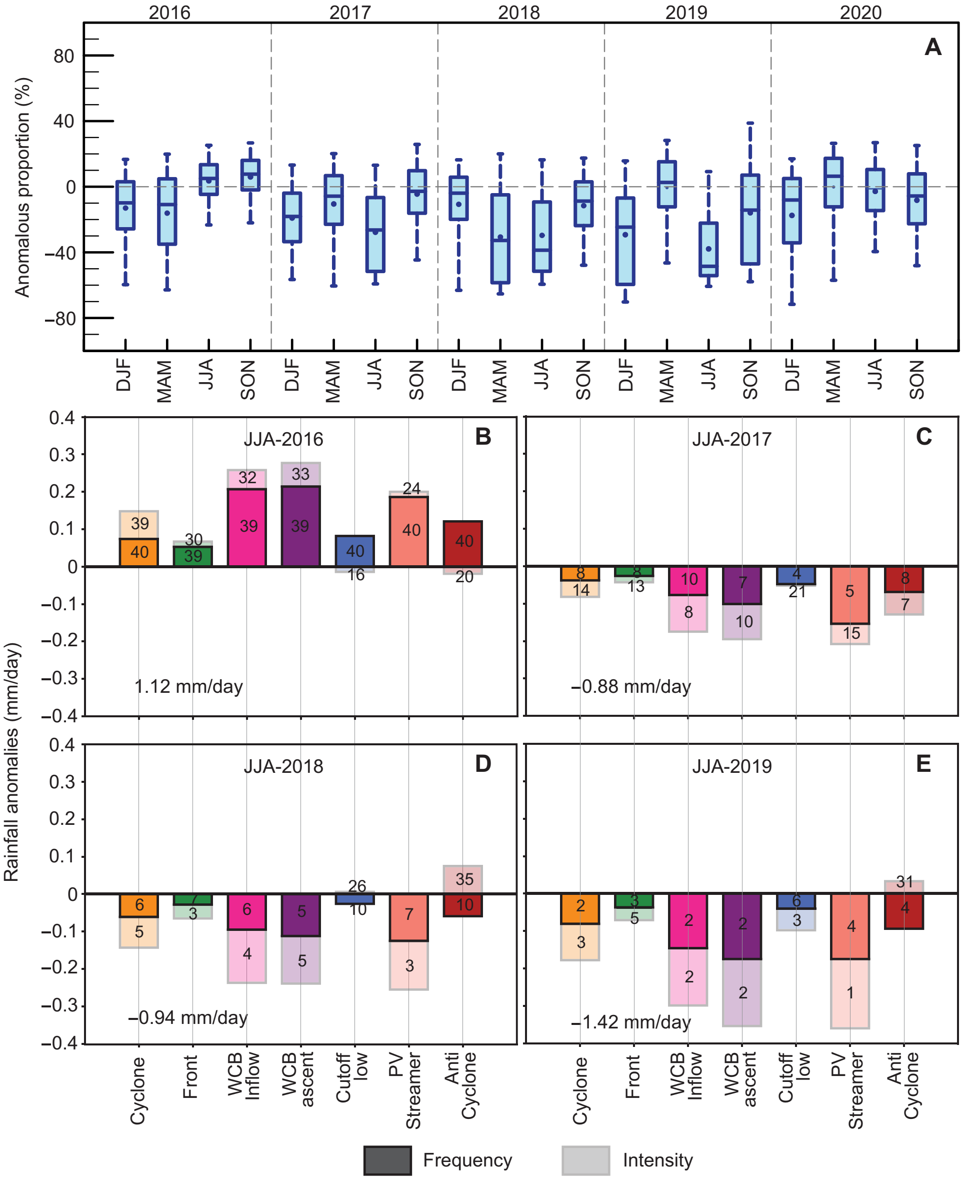

Fig. 8. Rainfall anomalies associated with heavy rainfall days and weather systems during the Tinderbox Drought. (**A**) The distribution of the anomalous proportion (%) of seasonal rainfall stemming from heavy rain days from DJF 2015/16 to SON 2020, computed for each grid box in the Tinderbox Drought domain. The anomalous proportion is defined as the proportion of the seasonal rainfall total that falls on days exceeding the climatological 90th percentile of rain days (>0.01 mm/day). Whiskers show the 5th/95th percentiles, the box shows the interquartile range, and the median and mean are denoted by the horizontal line and dot, respectively. For example, if the climatological mean contribution of heavy rain days to a seasonal rainfall total is 70% and during a given year of the drought it was 20%, the value shown is −50%. (**B** to **E**) The attribution of weather object frequency and intensity change to the daily rainfall anomalies (in mm/day) averaged over the Tinderbox Drought domain are shown for winter (JJA) of (B) 2016, (C) 2017, (D) 2018, and (E) 2019. Darker colored bars represent rainfall changes related to changes in object frequency, and the lighter shading to the intensity of rainfall associated with each object. The numbers within each bar are the rankings of the frequency and intensity anomalies compared to the full 40 years of data from 1980 to 2019, with 1 being the largest negative anomaly and 40 being the largest positive anomaly. The daily rainfall anomalies are calculated with respect to all winter days in the period 1980–2016. The numbers indicated in the bottom of (B) to (E) indicate the area mean rainfall anomaly for each JJA in mm/day equivalent.

Drought sensitivity in 2019 to other climate modes that are commonly associated with droughts in southeast Australia decreased for the IOD and slightly increased for SAM, yet both offered some predictability of the drought probability in 2019.

In contrast, the local climate, as represented by 3-month precipitation accumulation, soil moisture, ET, and PET, provided the most relevant information for predicting drought probability in 2019. For each of these local climate-based predictors, their importance to predictability of the Tinderbox Drought in 2019 was far greater than in other droughts of the past two decades. This may reflect the importance of land-atmosphere processes that intensified the Tinderbox Drought during its final year.

Overall, the machine learning method suggests that ENSO did not play a major role in predicting the likelihood of drought in 2019 (confirming our results from the section *Large scale climate drivers*). Instead, local climate features played the largest role in determining drought probability. This suggests that information from both large-scale climate drivers and local climate is necessary for accurate prediction of the conditions associated with the Tinderbox Drought in 2019.

Using the same RF approach, we quantified how the probability of drought derived from the local climate and the large-scale modes of variability evolved over time and space during 2016–2020 (fig. S11). In 2016, the prevailing climate conditions made drought less likely to occur during the winter and spring months (June to November). In contrast, climate conditions during the winters of 2017, 2018, and 2019 indicated a high likelihood (>0.5 and typically higher than 0.7) of drought. Between February 2019 and February 2020, the probability of drought was very high across the entire region (most months >0.7), in particular July to August 2019 and October 2019 to February 2020. The multivariate machine learning approach demonstrates that skillful prediction of the Tinderbox Drought was possible, even in the absence of extreme anomalies in a single predictor of drought.

Probability of drought breaking

Predicting when droughts are likely to end is also a critical aspect for adaptation responses to multi-year droughts. We examine another aspect of predictability by analyzing the influence of large-scale climate drivers on drought-breaking probabilities during the Tinderbox Drought. This draws on recent advances suggesting that the role of the major modes of variability in inhibiting drought-breaking rain, and thus allowing droughts to develop and continue, may be more important than their role in generating the dry conditions that lead to drought (*38*). Our results show that, in 2017, neither ENSO nor IOD contributed substantially to lower the probability of drought breaking. In 2018, ENSO contributed to some degree, and in 2019, IOD contributed more strongly to lowering the probability of drought breaking (Materials and Methods).

We use a logistic regression method (*54*) to estimate the probability of soil moisture drought breaking within the next 8 weeks during the Tinderbox Drought. The method estimates drought-breaking probabilities as a function of time of year, current soil moisture state, and ENSO and IOD, and has been shown to perform well in southeastern Australia (*54*). Soil moisture drought is defined based on percentile thresholds that vary by day of year. Figure S13 shows the area average probability (green line) and the area average probability contributions from the status of the climate modes (light and dark green shading) in the drought focus region for periods when more than half the grids in the Tinderbox Drought focus region experienced soil moisture drought. The status of the climate modes reduced the probability of drought breaking in the cool season.

There is a seasonal pattern in soil moisture drought spells in the drought focus region. More than half the grids in the region experienced soil moisture drought from July to October of all 3 years of the Tinderbox Drought, following the cool season deficits in rainfall (fig. S13, black line). More than half the grids also experienced soil moisture drought during some months in the warm seasons in 2019 and 2020 (January to March 2019, December 2019 to January 2020). In 2017, the probability of drought breaking was higher than 50%, and the states of ENSO and IOD did not contribute substantially to this probability. In the winters of 2018 and 2019, the probability of drought breaking was lower (around 40%). The main contributor to the lower probabilities of drought breaking was ENSO in 2018 and IOD in 2019. The state of the climate modes reduced the overall probabilities by 10 to 15%. The higher influence of IOD in 2019 from this method is consistent with the inference from the machine learning model for impact-based drought metrics. In contrast to the cool season, the probability contributions of the IOD and ENSO were minimal for drought spells during the warm periods in 2019 and 2020, resulting in drought-breaking probabilities that were high (≥60%).

The role of climate change in exacerbating the drought

The severity of the Tinderbox Drought and the different characteristics of this drought relative to previous droughts in southeast Australia lead to questions about the extent to which the Tinderbox Drought may have been worsened by human-caused climate change. The contribution of anthropogenic forcing to the Tinderbox Drought was estimated following the method described by Rauniyar and Power (*8*) using climate model simulations from the Coupled Model Intercomparison Project phase 6 (CMIP6).

We first estimated how unusual the rainfall anomaly observed during the Tinderbox Drought was in the context of unforced variability in preindustrial control simulations. Our results show that the observed 3-year cool season rainfall deficit during the Tinderbox Drought was unusually large compared to internal (i.e., unforced) model variability; it is estimated that there was only a 0.06% probability of occurrence of such an extreme rainfall deficit arising from modeled internal variability alone (Fig. 9C). This complements our earlier assessments (Fig. 5) that the rainfall deficits were also highly unusual compared to the expected range of internal variability based on historical observations. Such an anomalous rainfall deficit could be explained by the Tinderbox Drought being an exceptionally rare natural event (i.e., very bad luck), or an extreme event that has been exacerbated by anthropogenic forcing of the climate.

We estimated the contribution from anthropogenic forcing to the rainfall anomaly during the Tinderbox Drought by assessing 2017–2019 cool season rainfall anomalies for the drought region across future climate change scenarios (see Materials and Methods). The distribution of 3-year cool season rainfall anomalies simulated for 2017–2019 in the models demonstrates a negative shift relative to the distribution of unforced rainfall anomalies (Fig. 9A). The median percentage contribution of anthropogenic forcing to the observed cool season rainfall deficit during the Tinderbox Drought was 18.4% with an interquartile range of 34.9 to −13.3% across the multimodel ensemble. Assessment of the Millennium Drought in Victoria using the same method produced similar results, suggesting an ~20% anthropogenic contribution to the cool season drying that occurred during that event (*8*). These results are consistent with future climate change assessments suggesting that southeast Australia is likely to experience a long-term decline in cool season rainfall during the 21st century, but these assessments also currently have low confidence due to the large intermodel spread (*55*).

We do note, however, that even with the incorporation of anthropogenic forcing, very few CMIP6 simulations (3 out of 123) simulate 3-year cool season anomalies drier than −50%, and none are able to simulate the full magnitude of the observed deficit in rainfall during 2017–2019 (Fig. 9A). This remains true even if we account for interannual variability by examining the driest 3-year periods simulated by the models during the decade from 2014 to 2023

(Fig. 9B), rather than specifically 2017–2019 (Fig. 9A). In Fig. 9B, only one simulation is as dry as the observed rainfall deficit during the Tinderbox Drought and six simulations are drier than −50%. This suggests that in addition to anthropogenic intensification of the drought, the natural component of the Tinderbox Drought event was still highly unusual.

The rarity of CMIP6 simulations with 3-year cool season rainfall deficits as extreme as the Tinderbox Drought means that common event attribution methods are not able to be applied for the 2017–2019 event occurring during the decade surrounding it (Fig. 9, A and B). However, by instead interrogating a 20-year interval centered on the drought (2009–2028), the CMIP6 simulations yield nine 3-year periods as dry as the Tinderbox Drought from a total of 2460 samples across all scenarios. On the basis of this probability (0.37%) compared with the natural preindustrial probability (0.06%), the fraction of attributable risk for the Tinderbox Drought occurring during the 2009–2028 interval was 0.84. This suggests that climate change made the rainfall deficits of the Tinderbox Drought around six times more likely to occur than in preindustrial times.

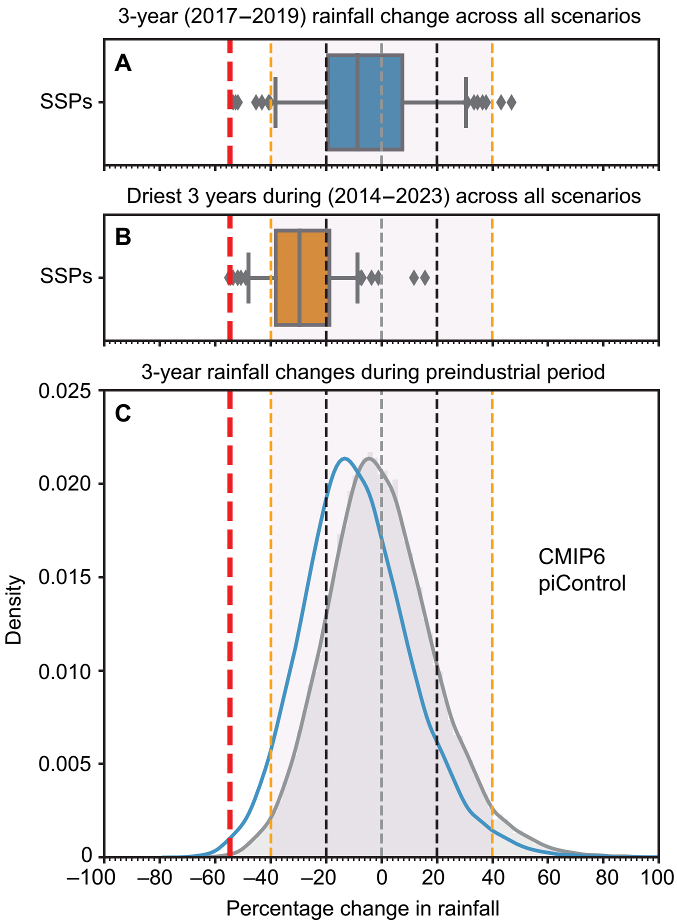

Fig. 9. Contribution of anthropogenic forcing. Percentage changes in area-averaged cool season rainfall of (**A**) the Tinderbox Drought (2017–2019) period, and (**B**) the driest 3-year period between 2014 and 2023 relative to the 1900–1959 period average in CMIP6 models. Box plots show the spread of change in rainfall based on historical simulations (to 2014) extended to year 2024 with 33 models under SSP5.85, 28 models under SSP3.70, and 31 models under SSP2.45 and SSP1.26 scenarios. We group all SSPs together for this analysis owing to the similarity of forcing in 2017–2019 across all scenarios. The vertical line in the box indicates the median, the box represents the interquartile range, and the whiskers indicate the 5th and 95th percentiles. (**C**) The range of a possible 3-year change due to internal variability alone based on CMIP6 models under preindustrial conditions. One and two SDs of the distribution due to internal variability alone are shown as vertical dashed lines in black and orange colors. The blue probability distribution is the same as the shaded curve, except that it is shifted left by the median value (i.e., our estimate of the externally forced response) of the box plot shown in (A). The observed % change is indicated using the thick vertical red dashed line in all panels.

An alternate approach presented in Fig. 9C further illustrates the combined internal and external factors involved in the Tinderbox Drought. The blue probability distribution in Fig. 9C is the relative frequency distribution of internal variability, after it has been shifted to the left (i.e., made drier) by the estimated externally forced response for 2017–2019 (i.e., a 10% cool season rainfall reduction, the median value in Fig. 9A). This shifted curve represents the modeled estimate of the relative frequency distribution of possible precipitation anomalies in the Tinderbox Drought region during 2017–2019, arising from both internal variability and external forcing, assuming that the shape of the tails of the rainfall distribution remain the same as the climate changes. The dry-shifted distribution has a larger tail area below the observed rainfall anomaly than the preindustrial distribution does (gray curve in Fig. 9C), but the probability of occurrence of the observed rainfall anomaly remains very small (0.45%) and consistent with the assessment of the fraction of attributable risk above. Taking the models at face value therefore suggests that the Tinderbox Drought was an extreme natural event that was made more likely and more intense by human-caused climate change.

DISCUSSION

Australia's Tinderbox Drought was a very extreme and impactful event. The drought encompassed meteorological, hydrological, and ecological/agricultural drought, causing sustained stresses on water resources and large decreases in agricultural yields leading to severe economic and societal impacts. It helped create favorable conditions for the most intense and widespread outbreak of forest fires ever recorded in southeast Australia, earning the name "Tinderbox Drought." Figure 10 summarizes the key characteristics, drivers, and impacts of the Tinderbox Drought.

The Tinderbox Drought was sustained and intensified across three consecutive years (2017–2019), characterized by an ~50% decline in cool season rainfall and a 15% decline in surface soil moisture from the 1980–2016 baseline (Figs. 3 and 10). While the rainfall anomalies were most pronounced during the cool season, there were also very few months of positive rainfall anomalies in the intervening warm seasons. As such, sustained declines of ET, streamflow, and water storage characterized the intensification of the Tinderbox Drought to its peak in the summer of 2019/2020. Temperature and VPD were also unusually high during the Tinderbox Drought, which amplified the drought impacts on vegetation, with widespread declines observed in vegetation cover during the drought (Figs. 3 and 4). The maximum temperatures during 2017–2019 were 1.6°C above the 1980–2016 baseline, and VPD was 15% higher than the 2002–2016 baseline.

Low rainfall and, more specifically, the absence of heavy rainfall events related to substantial declines in the intensity of rain-bearing systems, during the Tinderbox Drought was caused by oceanic moisture from the Tasman and Coral Seas being diverted away from southeast Australia and toward northern Australia (Figs. 7 and 10).

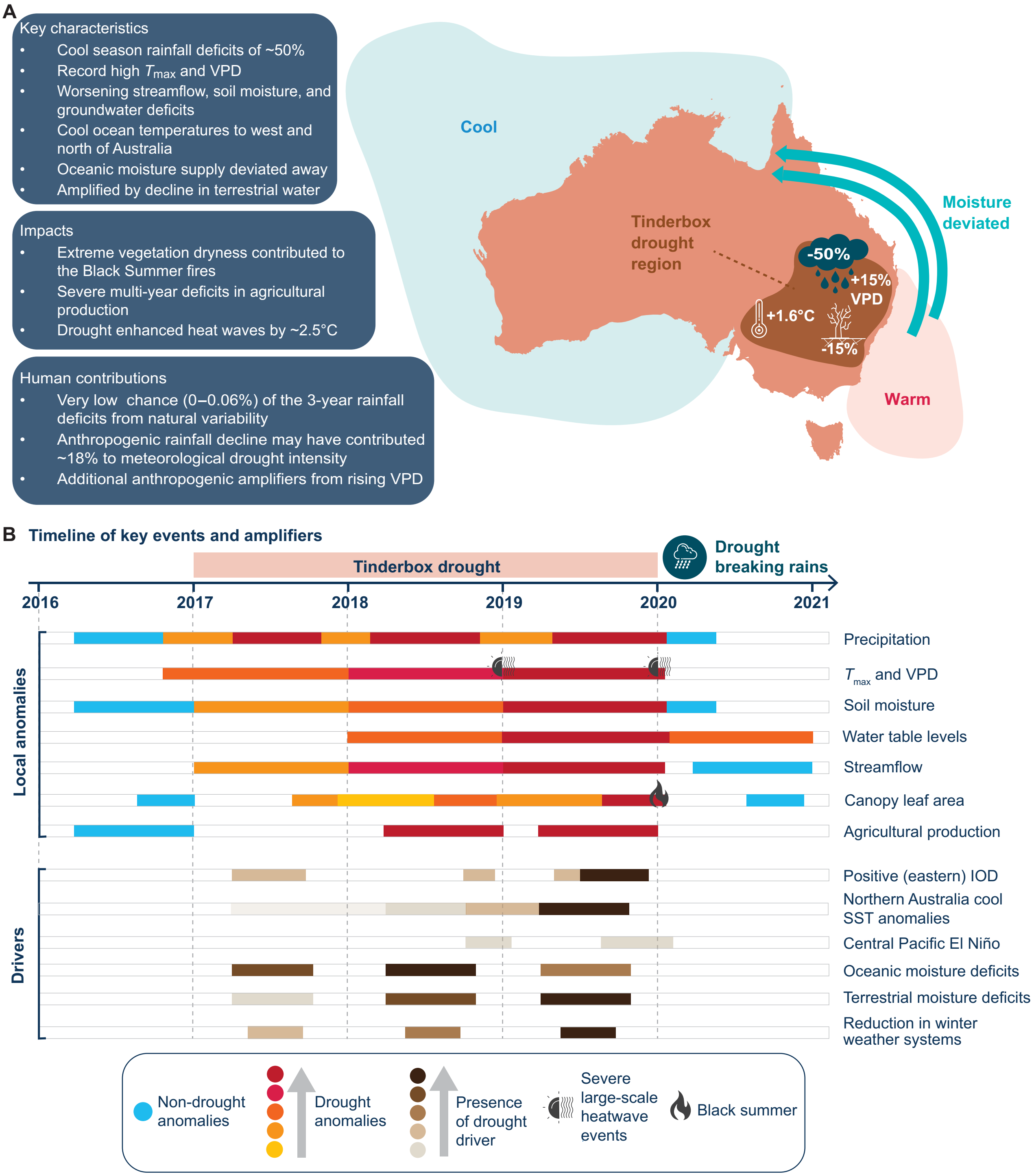

Key characteristics
- Cool season rainfall deficits of ~50%
- Record high $T_{\max}$ and VPD
- Worsening streamflow, soil moisture, and groundwater deficits
- Cool ocean temperatures to west and north of Australia
- Oceanic moisture supply deviated away
- Amplified by decline in terrestrial water

Impacts
- Extreme vegetation dryness contributed to the Black Summer fires
- Severe multi-year deficits in agricultural production
- Drought enhanced heat waves by ~2.5°C

Human contributions
- Very low chance (0–0.06%) of the 3-year rainfall deficits from natural variability
- Anthropogenic rainfall decline may have contributed ~18% to meteorological drought intensity
- Additional anthropogenic amplifiers from rising VPD

Fig. 10. Characteristics, drivers, and impacts of the Tinderbox Drought. (**A**) Map showing the area most affected by the drought, highlighting regions of warm and cool SST anomalies likely to have influenced the evolution of the drought. Aqua arrows show the path of moisture deflected away from the drought region, resulting in precipitation deficits. Graphics in the drought area show some of the major characteristics of the drought. (**B**) Timeline of key events and amplifiers of the drought, showing the magnitude of anomalies in relevant metrics (blue and warm colors), and the strength of remote climate drivers (browns). The intensity of shading indicates the strength of the respective drivers and anomalies.

While SST anomalies related to tropical climate variability are known to have strongly influenced past droughts in southeast Australia, ENSO did not play a role in the initiation of dry conditions during the Tinderbox Drought. Rather cool tropical SST anomalies to the north and west of Australia, including in the eastern region of the IOD, appear to have been more important in setting up the large-scale conditions that inhibited rainfall over southeast Australia in 2017–2019 (Fig. 6). After being initiated and sustained by remote oceanic conditions, local factors then acted to intensify the Tinderbox Drought and its impacts. Land-atmosphere feedbacks, which result from a strong association of dry and hot conditions in southeast Australia, amplified the intensity of heatwave events in 2018 and 2019 (Fig. 4 and fig. S10). Reduced water availability also resulted in a reduction of local moisture sources over the drought region in 2018 and 2019 (Fig. 7). Drought-breaking rainfall in February of 2020 ended the Tinderbox Drought, though some elements of the hydrological cycle still had not recovered to predrought levels almost a year after the meteorological drought broke (Fig. 3).

Climate variability in southeast Australia is high, and the region is renowned for its large swings between "drought and flooding rains," but evidence points to the Tinderbox Drought being more than just very bad luck. The Tinderbox Drought was exceptionally rare in its severity—in terms of both the 3-year mean rainfall deficit and in the occurrence of three consecutive dry years—against assessments of natural variability in observational data (Fig. 5) and climate simulations (Fig. 9). Studies have highlighted observed reductions to the frequency of fronts and cyclones, and increases in anticyclones over the region (*56*, *57*). Moreover, southeast Australia is expected to undergo sustained declines in cool season rainfall as climate change continues this century, causing a southward shift in rain-bearing Southern Ocean storms (*1*, *55*, *58*). Climate simulations suggest that human-caused drying may have already intensified the cool season rainfall deficits of the Tinderbox Drought by around 18% (Fig. 9). However, the Interquartile Range (34.9 to −13.3%) highlights the considerable uncertainty in this estimate, resulting from the inability of current climate simulations to accurately capture rainfall processes in our study region. This includes considerable intermodel spread in projected mean rainfall changes due to human-caused climate change, and limitations in model representations of multi-year drought due to a lack of persistence of simulated rainfall deficits (*2*) and systematic errors in land surface models (*58*). The observed linear decline in April to September rainfall since 1900 is not statistically significant, and it is expected that the length of the observational record is currently too short for significant anthropogenically forced differences in drought metrics to emerge (*59*). However, cool season rainfall this century (since 2000) has averaged 165 mm (±62 mm; 1σ) over the Tinderbox Drought region compared with an average of 192 mm (±63 mm; 1σ) during the 20th century. This ~14% reduction in rainfall is similar to the broader 10% decline in cool season rainfall that has occurred over southeast Australia (*24*). The observations are also consistent with the median 10% decline of cool season rainfall simulated across CMIP6 models for the 2017–2019 interval (Fig. 9A). Together, it appears likely that human-caused climate change played a role in worsening the rainfall deficits of the Tinderbox Drought.

There are also multiple other ways in which human-caused climate change may have worsened the Tinderbox Drought. Elevated temperatures over southeast Australia during 2017–2019 can be unequivocally linked to anthropogenic forcing (*1*, *24*), although the intensity of heatwaves later in this event were also amplified by the drought. The impacts of rising atmospheric temperature on increasing VPD provides a high-confidence mechanism for anthropogenic forcing to increase drought (and fire) risk (*28*) beyond the more direct climate change impacts on rainfall although the degree to which increasing VPD enhances these risks is poorly understood. Drought also feeds back to amplify VPD anomalies, and it is evident that land-atmosphere processes influenced the intensification of the Tinderbox Drought. Nevertheless, record-high VPD may have led to local intensification of the impacts of the Tinderbox Drought, something that sets this drought apart from historical conditions in southeast Australia (Fig. 4A). Drought monitoring also showed indicators of hydrological and agricultural drought emerging ahead of meteorological drought indicators. It is possible that this reflects the additional stress on these systems by elevated background temperature and VPD. It is also possible that the hydrological system in southeast Australia was already under stress from the multi-decade dry phase that preceded the Tinderbox Drought, including incomplete recovery from the multi-year Millennium Drought. Anthropogenic climate change is also thought to be altering the way tropical climate variability operates. Trends toward more frequent central Pacific–type El Niño events, and stronger and more frequent positive IOD events, are seen in paleoclimate and observational data, and these drought-promoting trends are projected to continue in the future as a consequence of human-caused climate change (*13*).

Some aspects of the Tinderbox Drought were unexpected. Our study shows that the traditional indices used to represent the tropical modes of variability may not be optimal for guiding the communication of seasonal outlooks of drought risk in southeast Australia. ENSO, as represented by the Niño3.4 index, provided far less predictive skill of the unfolding rainfall anomalies during the Tinderbox Drought than during previous drought events (fig. S12). The eastern pole of the IOD appears more important as a predictor than the full DMI, while tropical SSTs to the north of Australia appear to have more skill in determining cool season rainfall anomalies over our study region than any of the traditional climate mode indicators (Fig. 6). However, our study also highlights the importance of local climate factors in drought intensification and predictability. Furthermore, there are promising pathways forward for the skillful prediction of drought risk when multiple predictors are used simultaneously through machine learning approaches (fig. S12). This is particularly important as the Tinderbox Drought demonstrates that extreme and impactful droughts are able to develop without any particular indicator of drought risk being in an extreme state.

The Tinderbox Drought illustrates the necessity for multidisciplinary approaches in improving our understanding of the causes, impacts, and predictability of multi-year droughts. What is considered a single event can be associated with multiple interacting drivers and impacts that evolve during the event. Past research has tended to focus on understanding droughts and other climate extremes by a single explanation. This study demonstrates how drawing together a diversity of research expertise, and using powerful research tools including machine learning, can greatly advance our understanding of complex events. Extending this approach to other droughts in southeast Australia, and to multi-year droughts in other regions of the world, provides avenues to advance our understanding of past droughts and future drought risk.

Our study has demonstrated that the Tinderbox Drought was an extreme natural event that was likely worsened by human-caused climate change. Future projections of climate change indicate that in many regions of the world, including parts of our study region, climate change is expected to make droughts more frequent and more severe (*60*). However, there are serious limitations in the ability of current climate models to simulate multi-year droughts such as the Tinderbox Drought that hinders our understanding of the nature and drivers of Australian droughts. It is also evident that the observational record is not sufficient to capture the full range of possible natural variability in multi-year droughts. Continued quantification of the processes that interact to initiate, sustain, and end multi-year droughts, and improved representation of these processes in models, will be required to improve projections of future drought risk and support adaptation decisions. Although not quantified in our study, increasing human demand on water resources also represents a potential further anthropogenic component to the Tinderbox Drought. Changes in human demand for water are not readily incorporated into future projections of drought, but water management practices will be key to managing the risks of future multi-year droughts in southeast Australia and other drought-prone regions.

MATERIALS AND METHODS

Data

The datasets used for analyses are listed in table S1.

Drought metrics

We used standardized metrics and percentile thresholds to identify areas that experienced meteorological and agricultural/ecological drought during the years 2017 to 2019. Metrics based on precipitation, PET, and soil moisture from the multiple datasets listed in table S1 are used to calculate the drought metrics.

The Standardized Precipitation Index (SPI) (*61*) is an index that is widely used to characterize meteorological drought. SPI quantifies the deficit in accumulated precipitation in terms of probability on various timescales, typically between 1 and 36 months. To calculate SPI, a defined baseline record is fitted to a probability distribution (the gamma distribution) and transformed to a normal distribution. The SPI values are standard normal deviates, and the index indicates units of SD from the long-term mean. We assess deficits in precipitation using the 3-month SPI (SPI-3) values less than −1. The −1 threshold corresponds to moderate dryness (*61*). SPI-3 was calculated from three precipitation datasets (AGCD, MSWEPv2.8, and CHIRPS-2.0). The Australian Gridded Climate Data (AGCD) is a gauge-based product providing monthly and daily precipitation, temperature, and vapor pressure data at 0.05° × 0.05° spatial resolution (*62*). Multi-Source Weighted-Ensemble Precipitation (MSWEPv2.8) is a global gridded precipitation product that merges gauge, satellite, and reanalysis data at a spatial resolution of 0.1°. Climate Hazards Group InfraRed Precipitation with Station data (CHIRPS-2.0) is another merged product that incorporates satellite imagery and station data to create gridded precipitation data at 0.05° resolution between 50°N and 50°S.

The 3-month Standardized Precipitation Evapotranspiration Index (SPEI-3) (*63*), which includes the additional water balance component of PET, is used to identify areas in agricultural/ecological droughts using the same threshold of −1 from two sets of datasets. The Global Land Evaporation Amsterdam Model (GLEAMv3.5) provides estimates of actual and PET (AET and PET) globally at a spatial resolution of 0.25°. Historical estimates of AET and PET are provided from the Australian Water Resources Assessment Landscape (AWRA-L) model (*64*) at a spatial resolution of 0.05°. SPEI-3 is calculated using two sets of datasets: (i) precipitation from the AGCD and PET from AWRA-L, and (ii) precipitation from MSWEPv2.8 and PET from GLEAMv3.5. We also assess seasonal and annual precipitation accumulations and root zone soil moisture below the corresponding 15th percentile thresholds, which broadly corresponds to an SPI/SPEI of −1 and is chosen for consistency. The root zone soil moisture from GLEAMv3.5 and AWRA-L datasets are used for this assessment. All baseline calculations for SPI-3, SPEI-3, and the 15th percentile are for 1980 to 2016.

Calculation of hydrometeorological anomalies

We use gridded precipitation and actual ET from multiple datasets to estimate monthly and seasonal anomalies. We calculate the average precipitation anomalies from AGCD, MSWEPv2.8, and CHIRPS-2.0 datasets. We calculate average ET anomalies using estimates from AWRA-L and GLEAMv3.5. We also calculate maximum temperature anomalies from the AGCD dataset. Soil moisture from the European Space Agency Climate Change Initiative dataset is used to quantify anomalies in surface soil moisture. Monthly and seasonal anomalies in all variables are computed with respect to a baseline period of 1980 to 2016 for datasets except CHIRPS-2.0. A baseline of 1981 to 2016 is used for the CHIPRS-2.0 due to data availability constraints.

We also use shorter records from satellite datasets and field measurements to study changes in other water cycle variables during the drought. Total TWS anomalies from the GRACE data are used to study changes in deeper soil storages. Combined data from the GRACE and GRACE follow-on missions are available for the period 2002 to 2021 and we estimate monthly TWS anomalies with respect to a shorter baseline of 2002 to 2016. Because of the time lag between the two GRACE missions, TWS data during a year of the drought (mid 2017–2018) is missing from this dataset. Point measurements of streamflow and water levels in borewells are available at some locations in the region of interest. Streamflow data at high-quality hydrologic reference stations are available from BoM, and the length of the record varies by station. Here, we study anomalies in streamflow at stations that receive inflows from catchment areas larger than ~1000 km^2 (Fig. 1). Streamflow in the drought focus region is highly variable on short timescales. Most months have streamflow below the baseline (1980–2016) mean, interspersed with sporadic very high streamflow events. To better identify trends in streamflow during the Tinderbox Drought, we average the streamflow data to a seasonal resolution (Fig. 3E) instead of presenting monthly resolution data. We use borewell observations from the Australian groundwater explorer (*65*) to study changes in water table depth, after removing the measurements flagged as low quality. Borewell water level measurements that cover the region and period of interest are generally scarce, but some spatial clusters of data are available primarily for a shorter period from 2010 to 2021 (Fig. 1). Some clusters of borewells in Darling, Murrumbidgee & Upper Murray, Hunter & Namoi, Lachlan, Gwydir, and Condamine basin regions contain data that cover more than 80% of the period from 2010 to 2021. Hence, we estimate the monthly water level anomalies in these regions with respect to a shorter baseline of 2010 to 2016. The relatively slowly varying TWS and soil moisture anomalies are also estimated with respect to the same shorter baseline to present anomalies consistent with the changes in borewell water levels.

Calculation of vegetation-related anomalies

Vegetation anomalies were calculated with respect to 2002–2016, owing to data availability constraints from the satellite datasets. We calculated anomalies on remote sensing–derived data and VPD from the AGCD dataset using data from the satellite-derived estimates of VOD using the LPDR v3 product, which broadly corresponds with canopy water content; the NDVI from MYD13A2 collection 6.1, which is a well-known proxy of canopy area and vegetation productivity; and land skin temperatures from the MYD11A1 collection 6.1 product, which can serve to indicate departures in canopy latent heat flux due to changes in canopy transpiration. VOD and NDVI anomalies during spring (SON) were, on average, the most severe during the drought.

We obtained agricultural statistics from two datasets (listed in table S1) to assess the impact of the Tinderbox Drought on these crops. We use wheat and barley statistics from the Australian Bureau of Agricultural and Resource Economics and Sciences (ABARES) farm survey data reported for sub-regions within the drought focus region to estimate regional anomalies (https://agriculture.gov.au/abares/data/farm-data-portal). In the case of rice and cotton, sub-national statistics are not available. However, as most of the rice and cotton produced in Australia are grown in the Murray Darling Basin (*5*), we use national statistics from the United Nations Food and Agricultural Organization's Corporate Statistical Database (https://fao.org/faostat/en/#data/QCL) to assess the impact on these crops. The agricultural datasets are used to estimate the growing season anomalies in area harvested, crop yield, and agricultural production of these crops with respect to a baseline of 1990 to 2016. We use a shorter baseline due to data availability constraints in the ABARES farm survey dataset.

Linear inverse modeling

Multi-year seasonal precipitation deficits that contribute to droughts may occur due to natural variability, or require anthropogenic forcings. Determination of whether a particular drought is anomalous (and hence potentially anthropogenically forced) requires a long "baseline" against which to compare that event. We can estimate the long-term background (unforced) precipitation variability in climate models via long (hundreds of years) simulations with unchanging external forcings. However, we do not know how accurately climate models simulate long-term Australian precipitation variability, particularly in terms of extremes. The observational record of precipitation in southeastern Australia is not long enough to quantify the full natural range of precipitation variability, particularly in terms of the statistics of multi-year events (*31*, *33*).

Here, we use a recently developed approach that allows estimation of the full distribution of southeastern Australian precipitation variability, based on the spatial and temporal covariance structure of the observed climate system (assuming stationarity of these structures). Specifically, we assessed whether the 2017–2019 drought was unusual relative to a stochastically forced system with stationary statistics. We used LIMs to calculate an ensemble of precipitation trajectories that maintain the spatial and temporal correlation structure of the observational record. Our approach, based on (*66*) and (*67*), uses a LIM of the form

$$\frac{\mathrm{d}\mathbf{X}}{\mathrm{d}t} = \mathbf{L}\mathbf{X} + \zeta$$

where $\mathbf{X}$ is a state vector, $\mathbf{L}$ is a deterministic feedback matrix describing spatial and temporal autocorrelations, and ζ is a white noise term where data may be correlated in space but not time. To form $\mathbf{X}$, we used linearly detrended monthly global SST anomalies, and linearly detrended monthly precipitation amount anomalies over Australia. Inherent in this detrending step is the assumption that long-term trends have an anthropogenic component. We excluded the tropics due to the highly nonlinear precipitation. SST data were from two sources: the NOAA Extended Reconstructed SST V5 (ERSST), and the Centennial In Situ Observation-Based Estimates (COBE) listed in table S1. ERSST is available on an approximately 2° × 2° grid, spanning 1854 to present. COBE is available on a 1° × 1° grid, spanning 1891 to present. Both products are derived from observations from the International Comprehensive Ocean-Atmosphere Data Set. Precipitation data were from the AGCD. In both cases, we applied a 3-month running mean before construction of the LIMs, and clipped the SST data to 60°S to 60°N. As in (*67*), the precipitation portion of $\mathbf{X}$ was heavily down-weighted such that SST affects precipitation in $\mathbf{L}$, but precipitation does not affect SST. We ran each LIM version (one with SST from ERSST and one with SST from COBE) 100 times, for 117 years, resulting in 11,700 years of simulated 3-month–smoothed monthly precipitation variability driven by each SST product.

We used our LIM-derived estimate of long-term natural variability to calculate the probability of experiencing one, two, and three sequential years with precipitation deficits equal to or greater than the least severe deficit of the 3 years of the drought. For the annual-mean and April to September (AMJJAS), this was 2017. For DJF, this was 2018. This forms a null hypothesis against which to test the proposition that this drought occurred within the expected range of long-term natural variability.

Moisture tracking model

Southeast Australia's rainfall is affected by moisture supply from nearby oceans (*20*) and influenced by remote climate drives such as ENSO and IOD. Apart from the strong 2019 IOD that coincided with the late stages of the drought, the remote climate drivers could not fully explain the onset and development of the drought (*12*). Here, we look into local processes and explore the role of moisture sources and transport to the region as alternative mechanisms for understanding the genesis and evolution of the Tinderbox Drought.

We use the Lagrangian FLEXible PARTicle (FLEXPARTv9.0) dispersion model (*68*) to track water vapor in the atmosphere and identify the sources and sinks of moisture during the drought event. In this model, the global atmosphere is divided into approximately 2 million finite elements, called "particles," with constant mass transported using 3D wind fields. The model calculates changes in freshwater flux (evaporation, e, minus precipitation, p) associated with each particle for every time step, i.e., $e - p = m(\mathrm{d}q/\mathrm{d}t)$, where q is the specific humidity of each particle and m is the mass of the particle. The total (E − P) surface freshwater flux is then calculated by adding ($e - p$) for all the particles residing in the atmospheric column over a given area. Details of the model can be found in (*68*).

We use ERA-Interim Reanalysis to provide the 6-hourly data for winds and humidity at 61 atmospheric levels at 1° × 1° resolution. FLEXPART has been shown to provide a satisfactory representation of the hydrological cycle (*69*).

The Lagrangian model is integrated backward in time to identify the source regions that supply moisture for the precipitation over the region. The model is then integrated forward in time from the identified moisture sources to obtain the individual contribution from ocean and land to precipitation. The integration time is equivalent to the residence time of water vapor in the atmosphere and varies according to regions and seasons (*70*). For Australia, the optimum integration time is 6–10 days [(*71*); table S2].

Weather feature analysis

Weather feature datasets are used to investigate the behavior of weather systems over Australia to identify anomalous weather patterns during the drought. The datasets are established based on objective identification of weather or flow phenomena, and they allow analyzing the occurrence frequency, spatial distribution, and temporal variability of a specific weather system (*72*). Weather features are synoptic weather systems objectively identified in the ERA5 reanalysis, using the methods (*72*) applied to the ERA-Interim reanalysis. All weather or flow features are identified as hourly two-dimensional binary fields, with the value 1 representing the occurrence of the weather system at grid points and the value 0 indicating no weather system identified. A meaningful set of weather or flow phenomena that affect rainfall over the region of interest (Fig. 1) is selected in the analysis, including extratropical cyclones, fronts, and anticyclones [e.g., (*73*, *74*)]. In addition, warm conveyor belts, PV streamers, and cutoffs (indicating the Rossby wave breaking near the extratropical tropopause) are considered. Warm conveyor belts are the major precipitating part of extratropical cyclones (*75*), and PV streamers and cutoffs act as a precursor for heavy rainfall events [e.g., (*76*)]. The identification algorithms of cyclones, anticyclones, warm conveyor belts, and PV streamers and cutoffs are detailed in (*72*).

Whether the changes in rainfall are due to changes in the frequency and intensity of the rainfall from a particular weather system is investigated in a similar way to (*77*). We note that the rainfall attributed to each weather object does not amount to the total rainfall for that season for two reasons. The first is that rainfall is not exclusively attributed to an object, as weather objects can overlap with each other, reflecting the nature of co-occurrence of weather systems, such as PV streamers and cutoff lows. As a result, the relative contribution of overlapped weather objects to rainfall cannot be quantified. Second, it could be that no object described here was in the vicinity when rainfall was recorded, since there are likely to be other rainfall-producing processes not captured by the six weather objects. However, the vast majority of rainfall is accounted for by the weather objects examined.

Land-atmosphere model simulations

To analyze the impact of drought on summer temperatures and heatwave extremes, we implement the WRF-LIS-CABLE modeling system, which includes the Community Atmosphere Biosphere Land Exchange (CABLE) land surface model (LSM) and the National Aeronautics and Space Administration (NASA) Unified Weather Research and Forecasting (NU-WRF) model version 9.2. The version of CABLE LSM includes an explicit groundwater aquifer and has been evaluated at scales ranging from a site to global scales including for southeast Australia during the Tinderbox Drought (*78*). To obtain the equilibrated initial land states, we force the standalone CABLE LSM using the resampled 3-hourly AGCD dataset (*62*) for 90 years with fixed CO_2 concentrations, and then for the period 1970–2019 with varying CO_2 concentrations [see (*79*)].

We use the WRF atmospheric physics configurations suggested by Hirsch *et al.* (*80*) for southeast Australia. This includes the WRF Single-Moment 5-class microphysics scheme, the Mellor-Yamada-Janjic boundary layer and surface layer schemes, and the New Goddard shortwave and longwave radiation schemes. The simulations of the 2017–2019 drought (hereafter DROUGHT) are initialized using the equilibrated land conditions from the offline simulation on 30 November 2018 and on 30 November 2019, separately, and then run through the 2018/2019 and 2019/2020 summers forced by the ECMWF Reanalysis v5 (ERA5) dataset at 4-km resolution over southeast Australia. We also run a simulation with climatological soil moisture by using the 1970–1999 averaged soil and aquifer moisture on 30 November 2018 and 2019 (hereafter CLIM).

Impact-based drought indicators using machine learning

To complement the analyses of local hydrological variables and the large-scale modes of variability, we also examined what these climate features and their interactions can collectively tell us about the temporal and spatial development of this drought. To achieve this, we analyze written drought impact reports, noting the time, location of "drought" and "no drought" events, coincident climate conditions, and values of large-scale climate indicators. Then, using machine learning, we establish a predictive model of drought impact, based on climate conditions and large-scale climate modes as predictors.

We follow Hobeichi *et al.* (*53*), but develop an equivalent database of drought events for the region of interest in Australia. Monthly drought impacts reported by BoM, the NSW Department of Primary Industries, and NSW Department of Planning, Industry & Environment were used (table S4). Several local drought-related variables (precipitation, cumulative precipitation of current and two preceding months, soil moisture at root zone, ET, PET, deep drainage, and runoff) were used together with large-scale modes of climate variability (Niño 3.4 SST, IOD, and SAM) at monthly time steps as predictors for these events, simply labeled as binary "drought" or "no drought" events. In total, 935 labeled samples are used to train and validate a machine learning drought indicator, with the number of samples varying by year. Table S1 lists the data sources of the predictors.

The relationship was derived using an RF classifier (*81*) at a monthly timescale. The trained RF model, which we referred to as the "RF-drought indicator" was then used to calculate the probability of drought over the region of interest for 2016 to 2021. This allows us to build a nonlinear multivariate drought index that can predict the conditional probability of drought and also provide information about which predictors have the most predictive power in discerning "drought" and "no drought" events. The performance of the RF-drought indicator is tested using data not used for training. Using the RF model, we additionally perform a feature importance analysis to quantify the importance of each predictor in the model. We use this analysis to identify the drivers of the 2019 drought conditions, concentrating on this year due to a higher number of available samples from the impact reports.

Soil moisture drought-breaking probabilities

We apply the logistic regression method documented in (*54*) to estimate the probability of ongoing soil moisture drought events ending within the next 8 weeks. We use the results to assess the contributions of the climate modes to drought-breaking probabilities. We briefly summarize the method below and direct the reader to the original paper for more detail.

Soil moisture drought spells are identified using root zone soil moisture from the AWRA-L model historical dataset based on percentile thresholds calculated separately for each day of the year. A drought spell starts when the soil moisture falls below the 10th percentile and ends when it increases above the 30th percentile. The soil moisture change required to end an ongoing drought event is calculated as the amount of moisture change required to exceed the 30th percentile. Historical data are then used to estimate the probability of exceedance of the requisite soil moisture changes (i.e., the drought-breaking probability) as a function of the states of the climate modes. We use historical data from 1911 to 2016 to train the logistic regression models and estimate drought-breaking probabilities within 8 weeks. We also use the results to study the evolution of the contributions of ENSO and IOD to the drought-breaking probabilities.

Estimating the role of climate change

We used monthly precipitation for the first ensemble member (i.e., r1i1p1f1) of the preindustrial and historical experiment and four different future emission scenarios (see table S3 for the list of models used). The magnitude of the anthropogenic-forced drying in the 2017–2019 period in models is estimated by averaging the multimodel median (MMM) values across four emission scenarios, weighted by the number of models used under that scenario [see (*82*)]. Finally, the anthropogenically forced component is estimated by determining the proportional contribution of the averaged MMM value to the observed change. The interquartile range of the individual model estimates is also provided.

Supplementary Materials

This PDF file includes:

Supplementary Text
Figs. S1 to S13
Tables S1 to S4
References

REFERENCES AND NOTES

1. IPCC, Summary for policymakers, in *Climate Change 2021: The Physical Science Basis. Contribution of Working Group I to the Sixth Assessment Report of the Intergovernmental Panel on Climate Change*, V. Masson-Delmotte, P. Zhai, A. Pirani, S.L. Connors, C. Péan, S. Berger, N. Caud, Y. Chen, L. Goldfarb, M.I. Gomis, M. Huang, K. Leitzell, E. Lonnoy, J.B.R. Matthews, T.K. Maycock, T. Waterfield, O. Yelekçi, R. Yu, B. Zhou, Eds. (Cambridge Univ. Press, 2021), pp. 3–32.
2. S. I. Seneviratne, X. Zhang, M. Adnan, W. Badi, C. Dereczynski, A. D. Luca, S. Ghosh, I. Iskandar, J. Kossin, S. Lewis, F. Otto, I. Pinto, M. Satoh, S. M. Vicente-Serrano, M. Wehner, B. Zhou, Weather and climate extreme events in a changing climate, in *Climate Change 2021: The Physical Science Basis. Contribution of Working Group I to the Sixth Assessment Report of the Intergovernmental Panel on Climate Change*, V. Masson-Delmotte, P. Zhai, A. Pirani, S.L. Connors, C. Péan, S. Berger, N. Caud, Y. Chen, L. Goldfarb, M.I. Gomis, M. Huang, K. Leitzell, E. Lonnoy, J.B.R. Matthews, T.K. Maycock, T. Waterfield, O. Yelekçi, R. Yu, B. Zhou, Eds. (Cambridge Univ. Press, 2021), pp. 1513–1766.
3. X. Yuan, Y. Wang, P. Ji, P. Wu, J. Sheffield, J. A. Otkin, A global transition to flash droughts under climate change. *Science* **380**, 187–191 (2023).
4. B. Edwards, M. Gray, B. Hunter, The social and economic impacts of drought. *Aust. J. Soc. Issues* **54**, 22–31 (2019).
5. A. I. J. M. Van Dijk, H. E. Beck, R. S. Crosbie, R. A. M. De Jeu, Y. Y. Liu, G. M. Podger, B. Timbal, N. R. Viney, The millennium drought in southeast Australia (2001-2009): Natural and human causes and implications for water resources, ecosystems, economy, and society. *Water Resour. Res.* **49**, 1040–1057 (2013).
6. Z. Hao, V. P. Singh, Y. Xia, Seasonal drought prediction: Advances, challenges, and future prospects. *Rev. Geophys.* **56**, 108–141 (2018).
7. A. S. Kiem, F. Johnson, S. Westra, A. van Dijk, J. P. Evans, A. O'Donnell, A. Rouillard, C. Barr, J. Tyler, M. Thyer, D. Jakob, F. Woldemeskel, B. Sivakumar, R. Mehrotra, Natural hazards in Australia: Droughts. *Clim. Change* **139**, 37–54 (2016).
8. S. P. Rauniyar, S. B. Power, The impact of anthropogenic forcing and natural processes on past, present, and future rainfall over Victoria, Australia. *J. Clim.* **33**, 8087–8106 (2020).
9. D. G. C. Kirono, V. Round, C. Heady, F. H. S. Chiew, S. Osbrough, Drought projections for Australia: Updated results and analysis of model simulations. *Weather Clim. Extremes* **30**, 100280 (2020).
10. J. Lu, G. J. Carbone, J. M. Grego, Uncertainty and hotspots in 21st century projections of agricultural drought from CMIP5 models. *Sci. Rep.* **9**, 4922 (2019).
11. BoM, Special Climate Statement 70 update—drought conditions in Australia and impact on water resources in the Murray–Darling Basin (2019); http://bom.gov.au/climate/current/statements/scs70b.pdf.
12. H. Nguyen, M. C. Wheeler, H. H. Hendon, E.-P. Lim, J. A. Otkin, The 2019 flash droughts in subtropical eastern Australia and their association with large-scale climate drivers. *Weather Clim. Extremes* **32**, 100321 (2021).
13. N. J. Abram, B. J. Henley, A. Sen Gupta, T. J. R. Lippmann, H. Clarke, A. J. Dowdy, J. J. Sharples, R. H. Nolan, T. Zhang, M. J. Wooster, J. B. Wurtzel, K. J. Meissner, A. J. Pitman, A. M. Ukkola, B. P. Murphy, N. J. Tapper, M. M. Boer, Connections of climate change and variability to large and extreme forest fires in southeast Australia. *Commun. Earth Environ.* **2**, 8 (2021).
14. J. Lawrence, B. Mackey, F. Chiew, M. J. Costello, K. Hennessy, N. Lansbury, U. B. Nidumolu, G. Pecl, L. Rickards, N. Tapper, A. Woodward, A. Wreford, Australasia, in *Climate Change 2022: Impacts, Adaptation, and Vulnerability.Contribution of Working Group II to the Sixth Assessment Report of the Intergovernmental Panel on Climate Change*, H.-O. Pörtner, D.C. Roberts, M. Tignor, E.S. Poloczanska, K. Mintenbeck, A. Alegría, M. Craig, S. Langsdorf, S. Löschke, V. Möller, A. Okem, B. Rama, Eds. (Cambridge Univ. Press, 2022), pp. 1581–1688.
15. NSW DPI, NSW State Seasonal Update - December 2019 (ISSN 2202–1795 (Online). Volume 7 Issue 12, 2020); https://dpi.nsw.gov.au/climate-landing/ssu/december-2019.
16. S. Hatfield-Dodds, N. Hughes, A. Cameron, M. Miller, T. Jackson, Analysis of 2018 drought: 26 October 2018 (Australian Bureau of Agricultural and Resource Economics and Sciences, 2018).
17. Sydney Water, Water Conservation Report 2019–2020 (2020); https://sydneywater.com.au/content/dam/sydneywater/documents/water-conservation-report.pdf [Accessed 2023-04-11].
18. M. M. Boer, V. Resco de Dios, R. A. Bradstock, Unprecedented burn area of Australian mega forest fires. *Nat. Clim. Change* **10**, 171–172 (2020).
19. J. P. Evans, D. Argueso, R. Olson, A. Di Luca, Bias-corrected regional climate projections of extreme rainfall in south-east Australia. *Theor. Appl. Climatol.* **130**, 1085–1098 (2017).
20. C. M. Holgate, A. I. J. M. Van Dijk, J. P. Evans, A. J. Pitman, Local and remote drivers of southeast Australian drought. *Geophys. Res. Lett.* **47**, e2020GL090238 (2020).
21. NSW DPI, "NSW State Seasonal Update - January 2018" (ISSN 2202–1795 (Online) Volume 6 Issue 1, 2018); https://dpi.nsw.gov.au/__data/assets/pdf_file/0005/800744/nsw-state-seasonal-update-january-2018.pdf.
22. H. Nguyen, M. C. Wheeler, J. A. Otkin, T. Cowan, A. Frost, R. Stone, Using the evaporative stress index to monitor flash drought in Australia. *Environ. Res. Lett.* **14**, 064016 (2019).
23. R. C. McKay, G. Boschat, I. Rudeva, A. Pepler, A. Purich, A. Dowdy, P. Hope, Z. E. Gillett, S. Rauniyar, Can southern Australian rainfall decline be explained? A review of possible drivers. *Wiley Interdiscip. Rev. Clim.* **14**, e820 (2023).
24. BoM, State of the Climate 2022 (2022); http://bom.gov.au/state-of-the-climate/.
25. G. J. van Oldenborgh, F. Krikken, S. Lewis, N. J. Leach, F. Lehner, K. R. Saunders, M. van Weele, K. Haustein, S. Li, D. Wallom, S. Sparrow, J. Arrighi, R. K. Singh, M. K. van Aalst, S. Y. Philip, R. Vautard, F. E. L. Otto, Attribution of the Australian bushfire risk to anthropogenic climate change. *Nat. Hazards Earth Syst. Sci.* **21**, 941–960 (2021).
26. P. G. Jarvis, The interpretation of the variations in leaf water potential and stomatal conductance found in canopies in the field. *Philos. Trans. R. Soc. B Biol. Sci.* **273**, 593–610 (1976).
27. M. G. De Kauwe, B. E. Medlyn, A. M. Ukkola, M. Mu, M. E. B. Sabot, A. J. Pitman, P. Meir, L. A. Cernusak, S. W. Rifai, B. Choat, D. T. Tissue, C. J. Blackman, X. Li, M. Roderick, P. R. Briggs, Identifying areas at risk of drought-induced tree mortality across South-Eastern Australia. *Glob. Chang. Biol.* **26**, 5716–5733 (2020).
28. H. Clarke, R. H. Nolan, V. R. De Dios, R. Bradstock, A. Griebel, S. Khanal, M. M. Boer, Forest fire threatens global carbon sinks and population centres under rising atmospheric water demand. *Nat. Commun.* **13**, 7161 (2022).
29. AEGIC, Australian wheat (2022); https://aegic.org.au/wp-content/uploads/2022/09/AEGIC-Grain-Note-wheat-22_LR.pdf.
30. AEGIC, Australian barley (2022); https://aegic.org.au/wp-content/uploads/2022/09/AEGIC-Grain-Note-Barley_22.pdf.
31. M. Freund, B. J. Henley, D. J. Karoly, K. J. Allen, P. J. Baker, Multi-century cool- and warm-season rainfall reconstructions for Australia's major climatic regions. *Clim. Past* **13**, 1751–1770 (2017).
32. T. R. Vance, A. S. Kiem, L. M. Jong, J. L. Roberts, C. T. Plummer, A. D. Moy, M. A. J. Curran, T. D. van Ommen, Pacific decadal variability over the last 2000 years and implications for climatic risk. *Commun. Earth Environ.* **3**, 33 (2022).
33. M. Ho, A. S. Kiem, D. C. Verdon-Kidd, A paleoclimate rainfall reconstruction in the Murray-Darling Basin (MDB), Australia: 2. Assessing hydroclimatic risk using paleoclimate records of wet and dry epochs. *Water Resour. Res.* **51**, 8380–8396 (2015).
34. D. C. Verdon-Kidd, A. S. Kiem, Nature and causes of protracted droughts in southeast Australia: Comparison between the Federation, WWII, and Big Dry droughts. *Geophys. Res. Lett.* **36**, (2009).
35. W. Cai, A. Purich, T. Cowan, P. van Rensch, E. Weller, Did climate change–induced rainfall trends contribute to the Australian millennium drought? *J. Climate* **27**, 3145–3168 (2014).
36. C. C. Ummenhofer, M. H. England, P. C. McIntosh, G. A. Meyers, M. J. Pook, J. S. Risbey, A. S. Gupta, A. S. Taschetto, What causes southeast Australia's worst droughts? *Geophys. Res. Lett.* **36**, L04706 (2009).

37. C. C. Ummenhofer, A. S. Gupta, P. R. Briggs, M. H. England, P. C. McIntosh, G. A. Meyers, M. J. Pook, M. R. Raupach, J. S. Risbey, Indian and Pacific Ocean influences on Southeast Australian drought and soil moisture. *J. Climate* **24**, 1313–1336 (2011).
38. A. D. King, A. J. Pitman, B. J. Henley, A. M. Ukkola, J. R. Brown, The role of climate variability in Australian drought. *Nat. Clim. Change* **10**, 177–179 (2020).
39. N. Nicholls, Sea surface temperatures and Australian winter rainfall. *J. Climate* **2**, 965–973 (1989).
40. N. Nicholls, Local and remote causes of the southern Australian autumn-winter rainfall decline, 1958-2007. *Climate Dynam.* **34**, 835–845 (2010).
41. P. van Rensch, A. J. E. Gallant, W. Cai, N. Nicholls, Evidence of local sea surface temperatures overriding the southeast Australian rainfall response to the 1997–1998 El Niño. *Geophys. Res. Lett.* **42**, 9449–9456 (2015).
42. M. B. Freund, A. G. Marshall, M. C. Wheeler, J. N. Brown, Central Pacific El Niño as a precursor to summer drought-breaking rainfall over southeastern Australia. *Geophys. Res. Lett.* **48**, e2020GL091131 (2021).
43. H. H. Hendon, D. W. J. Thompson, M. C. Wheeler, Australian rainfall and surface temperature variations associated with the southern hemisphere annular mode. *J. Climate* **20**, 2452–2467 (2007).
44. E.-P. Lim, H. H. Hendon, G. Boschat, D. Hudson, D. W. J. Thompson, A. J. Dowdy, J. M. Arblaster, Australian hot and dry extremes induced by weakenings of the stratospheric polar vortex. *Nat. Geosci.* **12**, 896–901 (2019).
45. M. J. Pook, P. C. McIntosh, G. A. Meyers, The synoptic decomposition of cool-season rainfall in the southeastern Australian cropping region. *J. Appl. Meteorol. Climatol.* **45**, 1156–1170 (2006).
46. A. Pepler, Record lack of cyclones in southern australia during 2019. *Geophys. Res. Lett.* **47**, e2020GL088488 (2020).
47. T. Parker, A. J. E. Gallant, The role of heavy rainfall in drought in Australia. *Weather Clim. Extremes* **38**, 100528 (2022).
48. A. J. E. Gallant, D. J. Karoly, Atypical influence of the 2007 La Niña on rainfall and temperature in southeastern Australia. *Geophys. Res. Lett.* **36**, (2009).
49. J. S. Risbey, M. J. Pook, P. C. McIntosh, M. C. Wheeler, H. H. Hendon, On the remote drivers of rainfall variability in Australia. *Mon. Weather Rev.* **137**, 3233–3253 (2009).
50. S. H. Larsen, N. Nicholls, Southern Australian rainfall and the subtropical ridge: Variations, interrelationships, and trends. *Geophys. Res. Lett.* **36**, L08708 (2009).
51. H. Joos, M. Sprenger, H. Binder, U. Beyerle, H. Wernli, Warm conveyor belts in present-day and future climate simulations—Part I: Climatology and impacts. *Weather Clim. Dyn.* **4**, 133–155 (2023).
52. BoM, Australian long-range forecasts archive (2017); http://bom.gov.au/climate/ahead/outlooks/archive.shtml [Accessed 2023-06-13].
53. S. Hobeichi, G. Abramowitz, J. P. Evans, A. Ukkola, Toward a robust, impact-based, predictive drought metric. *Water Resour. Res.* **58**, e2021WR031829 (2022).
54. A. Devanand, J. P. Evans, G. Abramowitz, S. Hobeichi, A. J. Pitman, What is the probability that a drought will break in Australia? *Weather Clim. Extremes* **41**, 100598 (2023).
55. M. R. Grose, S. Narsey, F. P. Delage, A. J. Dowdy, M. Bador, G. Boschat, C. Chung, J. B. Kajtar, S. Rauniyar, M. B. Freund, K. Lyu, H. Rashid, X. Zhang, S. Wales, C. Trenham, N. J. Holbrook, T. Cowan, L. Alexander, J. M. Arblaster, S. Power, Insights from CMIP6 for Australia's future climate. *Earth's Future* **8**, e2019EF001469 (2020).
56. A. Pepler, P. Hope, A. Dowdy, Long-term changes in southern Australian anticyclones and their impacts. *Clim. Dyn.* **53**, 4701–4714 (2019).
57. A. S. Pepler, A. J. Dowdy, P. Hope, The differing role of weather systems in southern Australian rainfall between 1979–1996 and 1997–2015. *Clim. Dyn.* **56**, 2289–2302 (2021).
58. A. M. Ukkola, M. G. De Kauwe, M. L. Roderick, G. Abramowitz, A. J. Pitman, Robust future changes in meteorological drought inCMIP6 projections despite uncertainty in precipitation. *Geophys. Res. Lett.* **47**, e2020GL087820 (2020).
59. G. M. Falster, N. M. Wright, N. J. Abram, A. M. Ukkola, B. J. Henley, Emerging anthropogenic influence on Australian multi-year droughts with potential for historically unprecedented megadroughts. *EGUsphere* **1–32**, (2023).
60. H. Douville, K. Raghavan, J. Renwick, R. P. Allan, P. A. Arias, M. Barlow, R. Cerezo-Mota, A. Cherchi, T. Y. Gan, J. Gergis, D. Jiang, A. Khan, W. Pokam Mba, D. Rosenfeld, J. Tierney, O. Zolina, Water cycle changes, in *Climate Change 2021: The Physical Science Basis. Contribution of Working Group I to the Sixth Assessment Report of the Intergovernmental Panel on Climate Change*, V. Masson-Delmotte, P. Zhai, A. Pirani, S.L. Connors, C. Péan, S. Berger, N. Caud, Y. Chen, L. Goldfarb, M.I. Gomis, M. Huang, K. Leitzell, E. Lonnoy, J.B.R. Matthews, T.K. Maycock, T. Waterfield, O. Yelekçi, R. Yu, and B. Zhou (Eds.)], V. Masson-Delmotte, P. Zhai, A. Pirani, S. L. Connors, C. Péan, S. Berger, N. Caud, Y. Chen, L. Goldfarb, M. I. Gomis, M. Huang, K. Leitzell, E. Lonnoy, J. B. R. Matthews, T. K. Maycock, T. Waterfield, O. Yelekçi, R. Yu, B. Zhou, Eds. (Cambridge Univ. Press, 2021), pp. 1055–1210.
61. T. B. McKee, N. J. Doesken, J. Kleist, The Relationship of Drought Frequency and Duration to Time Scales in *Proceedings of the 8th Conference on Applied Climatology* (American Meteorological Society, 1993), pp 179–183.
62. D. A. Jones, W. Wang, R. Fawcett, High-quality spatial climate data-sets for Australia. *Australian Meteorological and Oceanographic Journal* **58**, 233–248 (2009).
63. S. M. Vicente-Serrano, S. Beguería, J. I. López-Moreno, A multiscalar drought index sensitive to global warming: The Standardized Precipitation Evapotranspiration Index. *J. Climate* **23**, 1696–1718 (2010).
64. A. Frost, A. Ramchurn, A. Smith, The Australian Landscape Water Balance model (AWRA-L v6) Technical Description of the Australian Water Resources Assessment Landscape model version 6 (2018).
65. BoM, Australian Groundwater Explorer web portal (2022); http://bom.gov.au/water/groundwater/explorer/map.shtml [Accessed 2022-08-06].
66. T. R. Ault, S. S. George, J. E. Smerdon, S. Coats, J. S. Mankin, C. M. Carrillo, B. I. Cook, S. Stevenson, A robust null hypothesis for the potential causes of megadrought in western North America. *J. Climate* **31**, 3–24 (2018).
67. S. Coats, J. E. Smerdon, S. Stevenson, J. T. Fasullo, B. Otto-Bliesner, T. R. Ault, Paleoclimate constraints on the spatiotemporal character of past and future droughts. *J. Climate* **33**, 9883–9903 (2020).
68. A. Stohl, P. James, A Lagrangian analysis of the atmospheric branch of the global water cycle. Part I: Method description, validation, and demonstration for the August 2002 flooding in Central Europe. *J. Hydrometeorol.* **5**, 656–678 (2004).
69. L. Gimeno, R. Nieto, A. Drumond, R. Castillo, R. Trigo, Influence of the intensification of the major oceanic moisture sources on continental precipitation. *Geophys. Res. Lett.* **40**, 1443–1450 (2013).
70. L. Gimeno, J. Eiras-Barca, A. M. Durán-Quesada, F. Dominguez, R. van der Ent, H. Sodemann, R. Sánchez-Murillo, R. Nieto, J. W. Kirchner, The residence time of water vapour in the atmosphere. *Nat Rev Earth Environ* **2**, 558–569 (2021).
71. R. Nieto, L. Gimeno, A database of optimal integration times for Lagrangian studies of atmospheric moisture sources and sinks. *Sci Data* **6**, 59 (2019).
72. M. Sprenger, G. Fragkoulidis, H. Binder, M. Croci-Maspoli, P. Graf, C. M. Grams, P. Knippertz, E. Madonna, S. Schemm, B. Škerlak, H. Wernli, Global climatologies of Eulerian and Lagrangian flow features based on ERA-Interim. *Bull. Am. Meteorol. Soc.* **98**, 1739–1748 (2017).
73. J. S. Risbey, P. C. McIntosh, M. J. Pook, Synoptic components of rainfall variability and trends in southeast Australia. *Int. J. Climatol.* **33**, 2459–2472 (2013).
74. A. S. Pepler, A. J. Dowdy, P. van Rensch, I. Rudeva, J. L. Catto, P. Hope, The contributions of fronts, lows and thunderstorms to southern Australian rainfall. *Climate Dynam.* **55**, 1489–1505 (2020).
75. K. A. Browning, Conceptual models of precipitation systems. *Weather and Forecasting* **1**, 23–41 (1986).
76. H. Wernli, M. Sprenger, Identification and ERA-15 climatology of potential vorticity streamers and cutoffs near the extratropical tropopause. *J. Atmos. Sci.* **64**, 1569–1586 (2007).
77. S. Clark, M. j. Reeder, C. Jakob, Rainfall regimes over northwestern Australia. *Q. J. Roy. Meteorol. Soc.* **144**, 458–467 (2018).
78. M. Mu, M. G. De Kauwe, A. M. Ukkola, A. J. Pitman, W. Guo, S. Hobeichi, P. R. Briggs, Exploring how groundwater buffers the influence of heatwaves on vegetation function during multi-year droughts. *Earth Syst. Dynam.* **12**, 919–938 (2021).
79. M. Mu, A. J. Pitman, M. G. De Kauwe, A. M. Ukkola, J. Ge, How do groundwater dynamics influence heatwaves in southeast Australia? *Weat. Clim. Extrem.* **37**, 100479 (2022).
80. A. L. Hirsch, J. Kala, C. C. Carouge, M. G. De Kauwe, G. Di Virgilio, A. M. Ukkola, J. P. Evans, G. Abramowitz, Evaluation of the CABLEv2.3.4 land surface model coupled to NU-WRFv3.9.1.1 in simulating temperature and precipitation means and extremes over CORDEX AustralAsia within a WRF physics ensemble. *J. Adv. Model. Earth Syst.* **11**, 4466–4488 (2019).
81. L. Breiman, Random forests. *Mach. Learn.* **45**, 5–32 (2001).
82. S. P. Rauniyar, S. B. Power, Estimating future rainfall distributions in a changing climate for water resource planning: Victoria, Australia. *Clim. Dyn.* **60**, 527–547 (2023).
83. G. J. van Oldenborgh, H. Hendon, T. Stockdale, M. L'Heureux, E. C. de Perez, R. Singh, M. van Aalst, Defining El Niño indices in a warming climate. *Environ. Res. Lett.* **16**, 044003 (2021).
84. H. E. Beck, E. F. Wood, M. Pan, C. K. Fisher, D. G. Miralles, A. I. J. M. van Dijk, T. R. McVicar, R. F. Adler, MSWEP V2 Global 3-hourly 0.1° precipitation: Methodology and quantitative assessment. *Bull. Am. Meteorol. Soc.* **100**, 473–500 (2019).
85. C. Funk, A. Verdin, J. Michaelsen, P. Peterson, D. Pedreros, G. Husak, A global satellite-assisted precipitation climatology. *Earth System Science Data.* **7**, 275–287 (2015).
86. J. Du, J. S. Kimball, Daily Global Land Surface Parameters Derived from AMSR-E and AMSR2, Version 3 (NASA National Snow and Ice Data Center Distributed Active Archive Center, Boulder, CO, USA, 2022), (available at http://dx.doi.org/10.5067/JIKQZ6WO5C5M [Accessed 2022-10-31]).
87. K. Didan, MODIS/Aqua Vegetation Indices 16-Day L3 Global 1km SIN Grid V061 (NASA EOSDIS Land Processes DAAC, 2021), (available at https://doi.org/10.5067/MODIS/MYD13A2.061 [Accessed 2022-10-31]).
88. Z. Wan, S. Hook, G. Hulley, MYD11A1 MODIS/Aqua Land Surface Temperature/Emissivity Daily L3 Global 1km SIN Grid V006 (NASA EOSDIS Land Processes DAAC, 2015), (available at https://doi.org/10.5067/MODIS/MYD11A1.006 [Accessed 2022-10-31]).

89. B. Martens, D. G. Miralles, H. Lievens, R. van der Schalie, R. A. M. de Jeu, D. Fernández-Prieto, H. E. Beck, W. A. Dorigo, N. E. C. Verhoest, GLEAM v3: Satellite-based land evaporation and root-zone soil moisture. *Geosci. Model Dev.* **10**, 1903–1925 (2017).
90. B. D. Tapley, S. Bettadpur, M. Watkins, C. Reigber, The gravity recovery and climate experiment: Mission overview and early results. *Geophys. Res. Lett.* **31**, (2004).
91. B. Huang, P. W. Thorne, V. F. Banzon, T. Boyer, G. Chepurin, J. H. Lawrimore, M. J. Menne, T. M. Smith, R. S. Vose, H.-M. Zhang, NOAA Extended Reconstructed Sea Surface Temperature (ERSST), Version 5 (NOAA National Centers for Environmental Information, 2017), (available at doi:10.7289/V5T72FNM. Obtain at NOAA/ESRL/PSD at their website https://esrl.noaa.gov/psd/).
92. M. Ishii, A. Shouji, S. Sugimoto, T. Matsumoto, Objective analyses of sea-surface temperature and marine meteorological variables for the 20th century using ICOADS and the Kobe Collection. *Int. J. Climatol.* **25**, 865–879 (2005).
93. D. P. Dee, S. M. Uppala, A. J. Simmons, P. Berrisford, P. Poli, S. Kobayashi, U. Andrae, M. A. Balmaseda, G. Balsamo, P. Bauer, P. Bechtold, A. C. M. Beljaars, L. van de Berg, J. Bidlot, N. Bormann, C. Delsol, R. Dragani, M. Fuentes, A. J. Geer, L. Haimberger, S. B. Healy, H. Hersbach, E. V. Hólm, L. Isaksen, P. Kållberg, M. Köhler, M. Matricardi, A. P. McNally, B. M. Monge-Sanz, J.-J. Morcrette, B.-K. Park, C. Peubey, P. de Rosnay, C. Tavolato, J.-N. Thépaut, F. Vitart, The ERA-Interim reanalysis: Configuration and performance of the data assimilation system. *Q. J. Roy. Meteorol. Soc.* **137**, 553–597 (2011).

Acknowledgments: This research was undertaken with the assistance of resources and services from the National Computational Infrastructure (NCI), which is supported by the Australian Government. **Funding:** This work was supported by Australian Research Council Centre of Excellence for Climate Extremes CE170100023 (A.D., G.M.F., Z.E.G., S.H., C.M.H., C.J., M.M., T.P., S.W.R., K.S.R., E.V., N.J.A., G.A., J.P.E., A.J.E.G., A.J.P., A.S.T., and A.M.U.), Xunta of Galicia (regional government) grant no. ED481B-2021/134 (M.S.), Australian Research Council Discovery Early Career Award DE200100086 (A.M.U.), and Australian Government's National Environmental Science Program, Community Grants Program, Activity ID 4-G47AV4M (N.J.A., J.P.E., A.J.E.G., and S.P.R.). **Author contributions:** Conceptualization: A.D., G.M.F., Z.E.G., S.H., C.M.H., T.P., S.W.R., M.S., N.J.A., G.A., J.P.E., A.J.E.G., A.J.P., A.S.T., A.M.U., S.P.R., and S.B.P. Investigation: G.M.F., E.V., Z.E.G., C.M.H., T.P., M.M., S.P.R., N.J.A., S.H., K.S.R., S.C., and S.W.R. Methodology: A.D., G.M.F., Z.E.G., S.H., C.M.H., C.J., M.M., T.P., S.W.R., K.S.R., M.S., E.V., N.J.A., G.A., S.C., J.P.E., A.J.E.G., A.J.P., S.B.P., S.P.R., A.S.T., and A.M.U. Resources: C.M.H., S.P.R., S.H., K.S.R., and S.W.R. Data curation: C.M.H., M.S., M.M., S.P.R., S.H., K.S.R., A.D., and S.W.R. Validation: C.M.H., M.S., T.P., S.P.R., S.H., K.S.R., A.D., and S.W.R. Formal analysis: A.D., G.M.F., Z.E.G., S.H., C.M.H., C.J., M.M., T.P., S.W.R., K.S.R., N.J.A., S.C., S.P.R., S.B.P., and A.S.T. Software: E.V., Z.E.G., C.M.H., M.S., T.P., M.M., S.P.R., S.H., K.S.R., S.C., A.D., and S.W.R. Visualization: A.D., G.M.F., Z.E.G., C.M.H., S.H., C.J., M.M., T.P., S.W.R., E.V., N.J.A., S.P.R., S.B.P., A.J.E.G., and A.S.T. Writing—original draft: A.D., G.M.F., Z.E.G., S.H., C.M.H., M.M., T.P., S.W.R., N.J.A., G.A., A.J.E.G., A.J.P., S.B.P., S.P.R., A.S.T., and A.M.U. Writing—review and editing: A.D., Z.E.G., S.H., C.M.H., S.W.R., E.V., N.J.A., G.A., S.C., J.P.E., A.J.E.G., A.J.P., S.B.P., S.P.R., A.S.T., and A.M.U. Project administration: A.D., A.J.P., G.A., and N.J.A. Funding acquisition: A.J.P., J.P.E., G.A., and N.J.A. Supervision: A.J.P., J.P.E., G.A., N.J.A., and A.J.E.G. **Competing interests:** The authors declare that they have no competing interests. **Data and materials availability:** The sources of the third-party data used for analyses are listed in table S1. Access to data is available upon registration through the listed third parties. The simulated datasets used in this paper are published in dryad repository 10.5061/dryad.12jm63z4q. The key scripts used for analyses available in the GitHub repository https://github.com/anjanadevanand/Tinderbox_drought is also archived in the dryad repository 10.5061/dryad.12jm63z4q. We use computer models available from third parties for analyses. The FLEXPARTv9.0 model used to understand the moisture sources is available from https://flexpart.eu/wiki/FpRoadmap. The WRF-LIS-CABLE modeling system used to model land-atmosphere coupling is based on NU-WRF model version 9.2 available from https://nuwrf.gsfc.nasa.gov/software upon registration. The instructions for coupling LIS with the CABLE land surface model is available at https://bitbucket.org/ahirsch/templates/wiki/Instructions. All data needed to evaluate the conclusions in the paper are present in the paper and/or the Supplementary Materials.

Submitted 22 June 2023
Accepted 29 January 2024
Published 6 March 2024
10.1126/sciadv.adj3460